Separation Control using Plasma Actuators: Experimental Studies of Plasma Actuator Performance

A THESIS
SUBMITTED TO THE FACULTY OF THE GRADUATE SCHOOL
OF THE UNIVERSITY OF MINNESOTA
BY

DartKen Poon

IN PARTIAL FULFILLMENT OF THE REQUIREMENTS
FOR THE DEGREE OF
MASTER OF SCIENCE

Uwe Kortshagen, Douglas Ernie

January, 2011

Acknowledgements

The present thesis is the summary of three years of working. I would like to dedicate this thesis to all the people who helped me throughout out the years.

First of all I would like to thank my advisors, Prof. Uwe Kortshagen and Prof. Douglas Ernie, for the amount of time they spent on me. I deeply appreciate them for their patience and time to help me throughout these three years. They redirected me when I lost direction. I learned so much more than just what this thesis presented, such as how to approach a problem, how to critical think, and how to present. Their help made my master studies a unique and unforgettable learning experience.

I would also like to thank everyone in this plasma actuator research group, including Prof. Terry Simon, Meenkashi Mamunuru, Song Guo, Debashish Burman, along with my advisors, for they gave me many helpful suggestions and critical feedback on my research. Gaung Yang also helped me with the initial design of the experimental system which really accelerated my learning curve when I first started the project. Prof. Kortshagen's research group also helped me a lot with my master study, especially Dave Rowe, who has helped me countless times when I was lost.

My family and my friends around the world deserve the biggest acknowledgments: thank you for your support. They are really important to me and I truly appreciate them. Without your support I would not be able finish this. Thank you so much.

Abstract

The characteristics of Dielectric Barrier Discharge (DBD) plasma actuators as active flow control devices were studied in this thesis. To determine the effectiveness of plasma actuators for various plasma actuator configurations, an experimental system was designed that included the ability to perform current-voltage characteristic and power measurements, thrust measurements, and optical measurements. Variations in plasma actuator configurations investigated included electrode gap distance, electrode shape, and dielectric thickness. Experiments showed that dielectric thickness has the most significant effect on the plasma actuator performance compared to the other factors studied. ICCD camera visualization studies of the discharge indicated that the degree of discharge asymmetry between the two current half cycles is linearly related to the thrust. A simple model was used to explore the relationships between the applied voltage V, plasma length L, and dielectric thickness T under constant power conditions. The resulting relationship $V^2 L \propto T$ derived from this model agreed well with the experimental results. Initial experiments were also performed on the effectiveness improvement capabilities of plasma actuators constructed using micro-scale exposed electrodes, with recommendations for their further study.

Table of Contents

List of Tables

List of Figures

Chapter 1. Introduction

Due to growing interest in energy conservation, scientists and engineers have been seeking methods for improving the efficiencies of energy systems of all kinds. In the area of fluid mechanics, finding new methods for improving aerodynamics could lead to a higher efficiency of current aircraft gas turbine engines. In a gas turbine engine, low pressure turbine efficiency has significant impact on the fuel consumption, as 1% improvement of the low pressure turbine efficiency could improve the fuel consumption by 0.5%-1%. For large aircraft applications, this 1% fuel consumption could save up to $200,000 per aircraft per year [1]. Flow separation is one of the main issues that limits the low pressure turbine efficiency. Thus, one method to increase the low pressure turbine efficiency is to reduce the flow separation through active flow control, such as dielectric barrier discharge plasma actuator. In this chapter, active flow control, dielectric barrier discharge and plasma actuator will be further explained.

1.1 Active flow control

In order to understand active flow control, first we need to understand what flow control is. Flow control is an aerodynamics improvement technology. It can be found in everyday life, with the most well-known example being the surface of the golf ball. Below is a demonstration of the basic concept of flow control. In Figure 1.1, we show two balls in a flow, one with a smooth surface, another one with dimples on the surface. In the real world, there is friction on every surface despite how smooth it is. The friction will cause the flow to lose momentum, which leads to insufficient kinetic energy for the flow to stay attached. Thus, a flow separation region, or wake, is created. This wake region will lead to a pressure difference between the upstream region and the downstream regions of the ball, causing a pressure drag. The smooth surface in this case has a laminar boundary layer at the point of separation, whereas the golf ball dimples disturb the flow and enable

transition from a laminar boundary layer to a turbulent boundary layer. Since the turbulent boundary layer has more “near-wall” momentum associated with it, it is able to follow the surface further before separation and, thus, has a smaller separation zone. In other words, the golf ball dimples reduce the drag force of the golf ball which enables the ball to travel further. The golf ball dimples are an example of *passive* flow control.

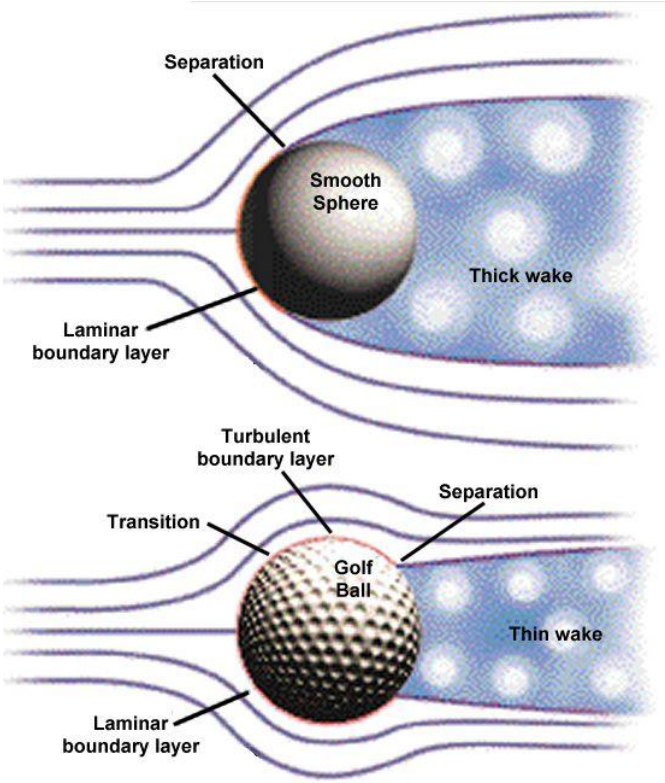

Figure 1.1: Flow separation with a laminar versus turbulent boundary layer [2]

Similarly, flow control technologies can be used to improve the aerodynamics of aircraft wings, or gas turbine airfoils. In a gas turbine engine, particularly in the low pressure turbine region, separation of the boundary layer may cause a significant amount of pressure drag. This is caused by the low Reynolds number in this region, as demonstrated in Figure 1.2. Figure 1.3 demonstrates that a low Reynolds number has a higher loss coefficient due to the flow separation. Thus, with the implementation of flow control, the efficiency of gas turbines could be

increased. This implies better performance of the gas turbine, improving the fuel efficiency as well as lowering emissions.

The engine that benefits from flow control under cruise conditions may not need flow control at take-off conditions. Thus, passive flow control is not desirable. Passive flow control cannot be deactivated when the control is not required. The difference between a *passive* control and *active* control is that the latter can be optimized in response to particular need for it. Since flow conditions in the gas turbine are variable, active flow control would be more practical.

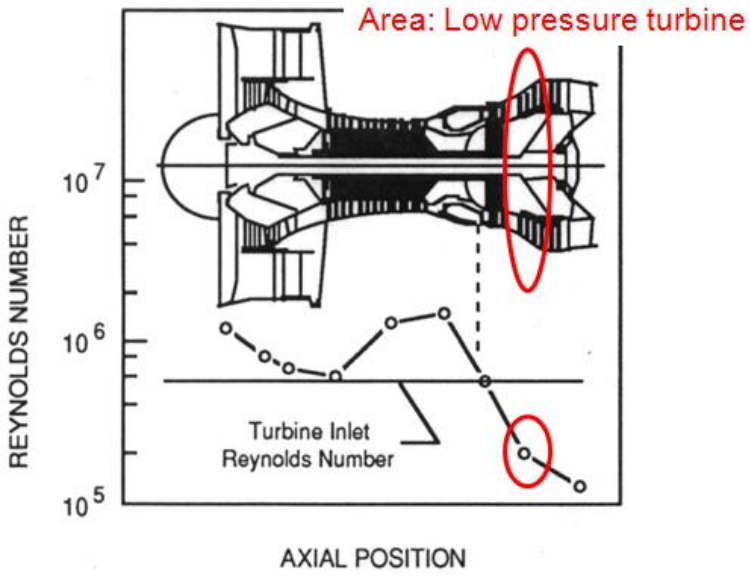

Figure 1.2: Reynolds number variation through out the engine [3]

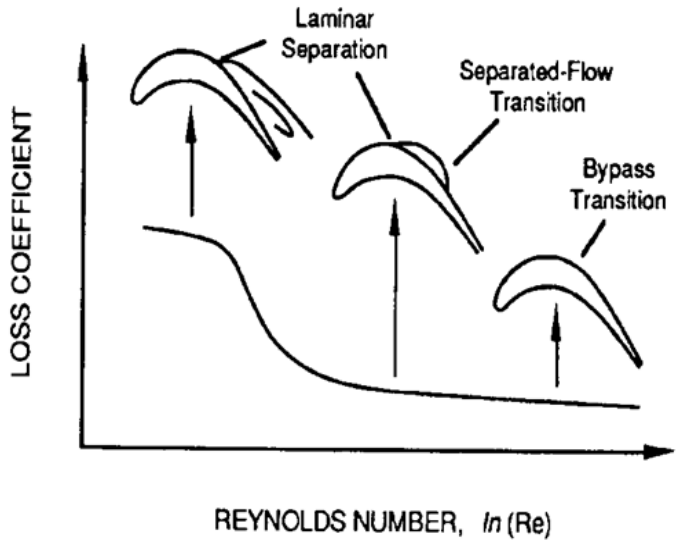

Figure 1.3: Transition on a low pressure turbine airfoil at various chord Reynolds numbers [3]

One example of active flow control is via synthetic jets. The synthetic jet is produced by modifying the airfoil as shown in Figure 1.4. A cavity is created which holds a diaphragm that, when activated, creates a jetting flow intermittent with a suction flow. The synthetic jet flow mixes with the main flow to promote transition. However, methods such as synthetic jets require mechanical parts and subsequently the airfoil would need to be modified. Recently, plasma actuators have gained more attention as an active flow control technology. The main benefit of plasma actuators is that they can transfer momentum to the flow without adding any mechanical parts on the airfoil. Plasma actuators ionize the air around the airfoil and use the generated ions to disturb the flow and induce transition. In this case, the plasma generated is called Dielectric Barrier Discharge (DBD), which will be further explained in the next section.

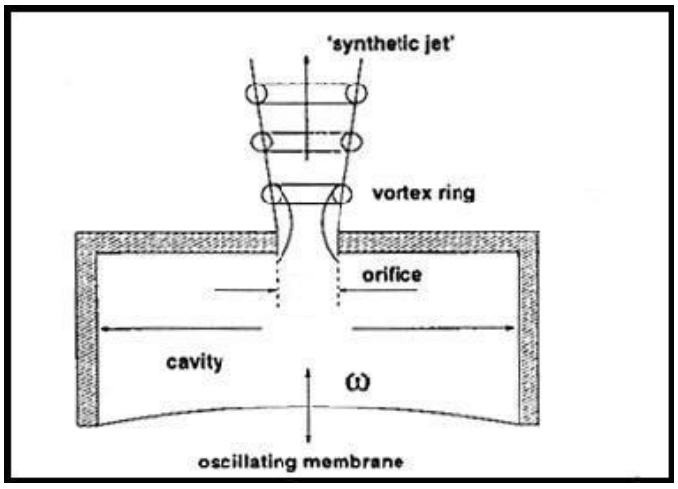

Figure 1.4: Synthetic jet actuators [4]

1.2 Dielectric barrier discharges

Dielectric barrier discharge was first introduced for the application of ozone generation by W. Siemens in 1857 [5]. Siemens' dielectric barrier discharge was a non-thermal, atmospheric pressure, plasma discharge. A DBD can be generated when there are one or more dielectric barriers between two electrodes across which a high voltage is applied. The purpose of the dielectric barrier is to limit the current and prevent the plasma from arcing. Some common dielectric barrier discharge configurations are shown in Figure 1.5. As shown in this figure, it is common to use AC power to operate DBDs with frequencies of the applied voltage varying between 500 Hz to 500 kHz [6].

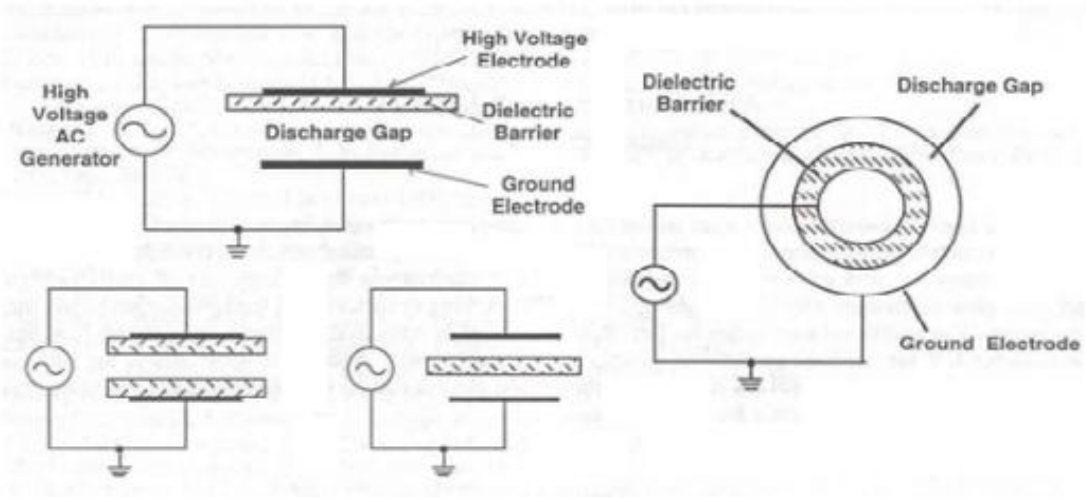

Figure 1.5: Common Dielectric Barrier Discharge Configurations [7]

As Figure 1.5 shows, dielectric barrier discharges can have various geometries, as needed for different applications. For example, a coaxial dielectric barrier discharge is typically used for ozone generation of water purification [8]. As for a plasma excimer lamp, both coaxial and planar dielectric barrier discharges could be used [9].

One of the unique properties of a DBD is its microdischarge mechanism, which involves numerous streamer-like micro-scale breakdown channels. Like most other plasmas, dielectric barrier discharges are initiated from a Townsend breakdown. An initial electron is accelerated by the applied external electric field and is used to ionize other atoms, creating more electrons. Those electrons then ionize more atoms inside the gap, creating an electron avalanche, as demonstrated in the Figure 1.6a. The ions move relativity slowly compared to the electrons, causing a positive space charge to develop within the avalanche. When the internal electric field of the avalanche generated by this space charge is comparable with the external field, it will cause the transformation from avalanche to streamer as shown in Figure 1.6b. The streamer, with the ions in front, will continue propagating from the anode until it reaches the cathode. This weakly ionized channel is called a streamer.

Once the streamer reaches the cathode, intense current will flow through this ionized channel, forming a microdischarge as shown in Figure 1.6c. However, if either or both electrodes are covered with a dielectric material, this dielectric barrier will prevent the charge carriers from reaching the electrodes and flowing into the external circuit. The charge carriers will accumulate on the dielectric resulting in a surface charge, as shown in Figure 1.6c, the electrons accumulate on the anode. This will reduce the electric field between the electrodes, preventing further growth of the microdischarge and the development of new avalanches and streamers nearby. At some point, the electric field between the electrodes is reduced by this surface charge to a level that is no longer high enough to sustain the needed electron impact ionization, and the microdischarge is then terminated. However, if the applied voltage from the power source is AC, the anode and cathode will be reversed each half cycle and the whole microdischarge process can be repeated each half cycle.

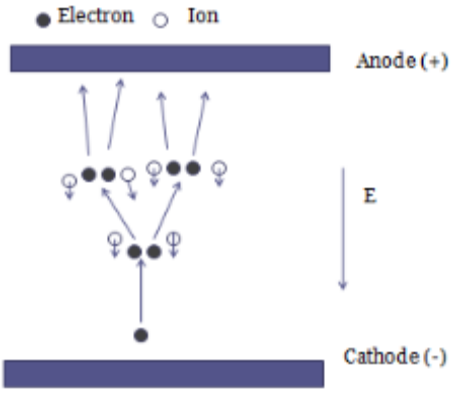

Figure 1.6a: Townsend breakdown initiated

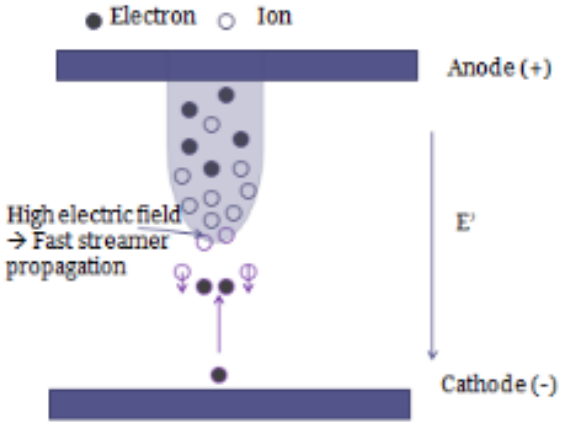

Figure 1.6b: Streamer formation

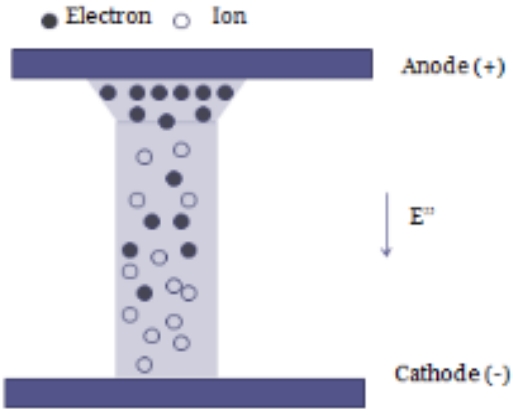

Figure 1.6c: Microdischarge formation

Typical parameters for a microdischarge are shown in Table 1.1. The microdischarge lifetime is relativity short; therefore, the AC frequency is generally held around 500 Hz to 500 kHz. Also, note that the peak current is about 0.1 A. This current limitation prevents arc formation between the two electrodes.

Table 1.1: Typical parameters of microdischarge [6]

Lifetime	1–20 ns	Filament radius	50–100 μm
Peak current	0.1 A	Current density	0.1–1 kA cm^{-2}
Electron density	10^{14}–10^{15} cm^{-3}	Electron energy	1–10 eV
Total transported charge	0.1–1 nC	Reduced electric field	$E/n = (1–2)(E/n)_{\text{Paschen}}$
Total dissipated energy	5 μJ	Gas temperature	Close to average, about 300 K
Overheating	5 K		

As a result of the self limiting nature of the microdischarge in a DBD configuration, instead of a single localized strong conducting channel (an arc) forming, transient microdischarges spread over the entire electrode surface with relative uniformity, as shown in Figure 1.7. This property allows plasma to be generated uniformly under atmosphere pressure. These unique properties of a DBD allow it to be used widely in industry. Besides the original application of ozone generation, other applications have been explored, such as excimer lamps and pollution control, as mentioned earlier. Using DBD for flow control has became recent application.

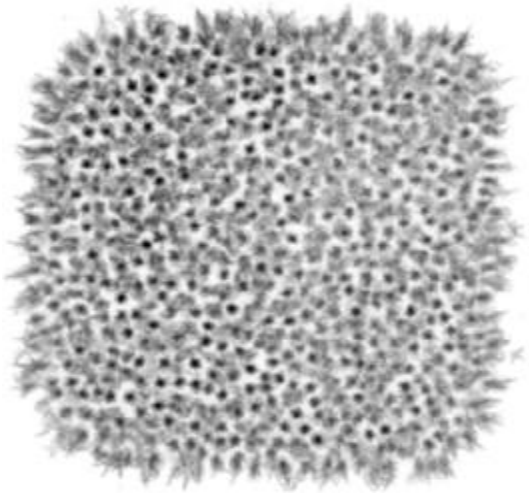

Figure 1.7: Image of filaments in DBD gap in air of a discharge gap of 0.762 mm, the discharge area is 5 cm × 5 cm [6]

1.3 Plasma actuator

Several previous studies have focused on the use of plasma actuators for active separation flow control on airfoils [10]. A plasma actuator is an electronic device that uses a dielectric barrier discharge to generate thrust which selectively adds momentum to fluid flow over a surface to affect flow separation. This is demonstrated in Figure 1.8, as the plasma actuator is activated, the flow reattaches to the airfoil. As shown in the figure, a plasma actuator could be imbedded into the airfoil and occupies little space. Also, the mechanism of the plasma actuator is relatively simple.

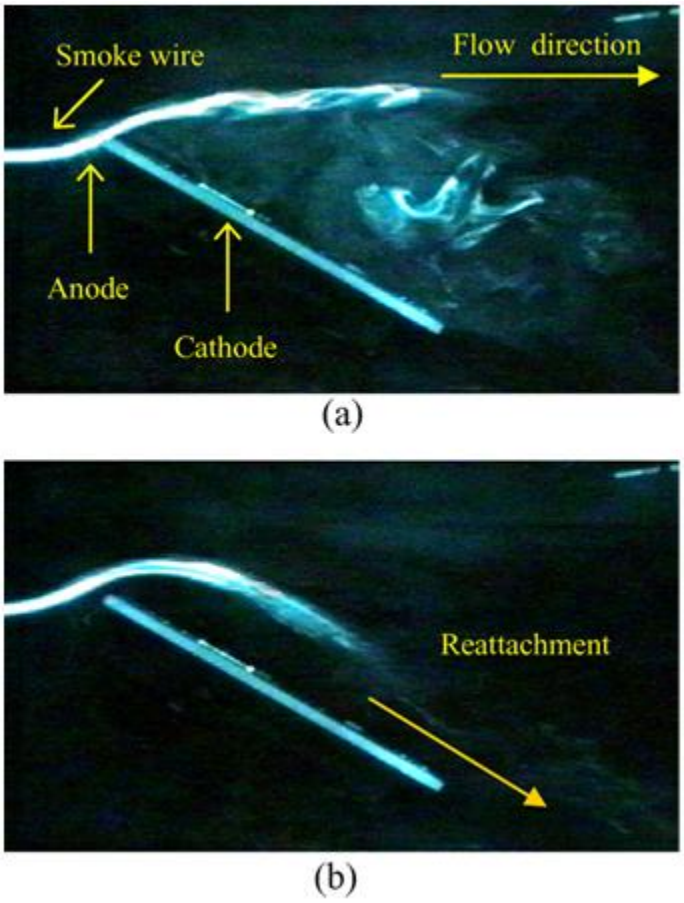

Figure 1.8: Plasma actuator effect on the airflow of at 0.4m/s, (*a*) plasma actuator off and (*b*) plasma actuator on. [10]

A typical plasma actuator design is shown in Figure 1.9. A simple plasma actuator consists of two offset metal electrodes, an exposed electrode and a covered electrode, and a dielectric, where the offset geometry is used to generate a one way net thrust. Plasma actuators can be constructed with various dielectric materials, such as aluminum oxide (ceramics), polyester, glass, etc., and with different dielectric thickness. For the electrodes, copper is typically used because of its high electrical conductivity. The electrodes can have various shapes, including thin strip and wire profiles, and various sizes. Thus, the geometry of the plasma actuator is not fixed but can be modified to improve its performance. Normally, the back side of the plasma actuator is covered with an insulated coating, such as Kapton (polyimide) tape, to prevent discharge on the back side. Thus, when a large AC voltage is applied across the actuator, the DBD would ideally be generated on only the exposed electrode.

Recently, simulations have been done trying to understand the physics behind the plasma actuator's DBD. Reactions with electron, ion-neutral, and neutral-neutral reactions were studied with various gas chemistry components present in air [11-15]. It is generally believed that the generated "thrust" from the plasma actuator is due to the collisions between the ionized gas and the neutral particles [10, 16]. It is found also that the configuration of the plasma actuator has a great effect on the generated thrust. For example, Thomas et al. showed that the generated thrust is correlated to the applied voltage frequency [17], Forte el al. demonstrated that the electrode gap distance has an effect on the generated thrust [18] and Enloe et al. showed that there was a relation between the electrode geometry and generated thrust [19]. Finding new ways to improve the plasma actuator performance is a popular research topic.

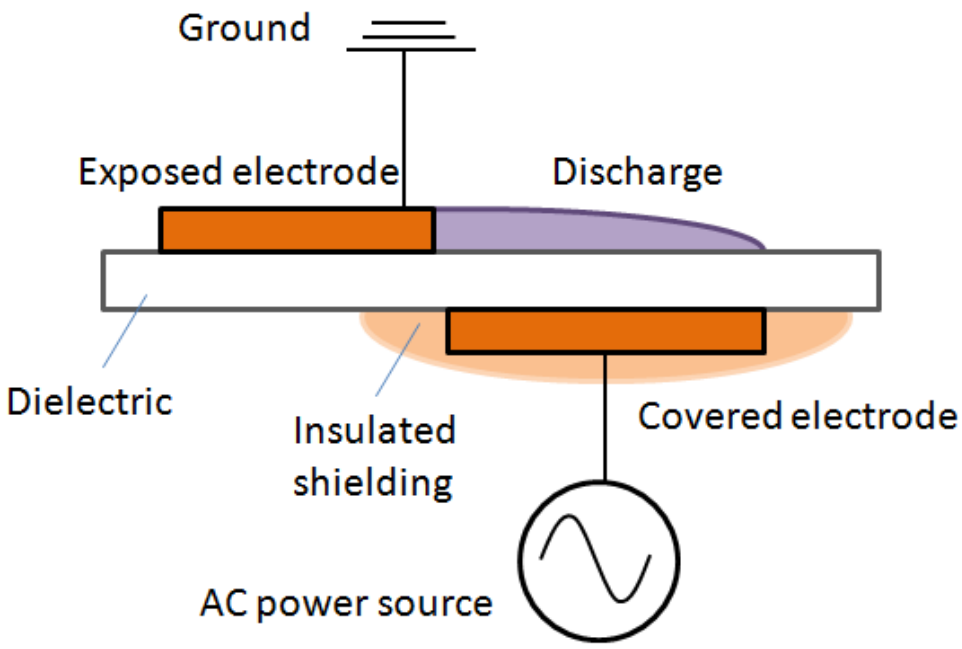

Figure 1.9: Schematic view of typical plasma actuator components

1.4 Objective

Throughout the literature, numerous of studies have shown that the configuration of the plasma actuator is a major factor affecting the generated thrust; however, very few have discussed the “effectiveness” of the plasma actuator, where effectiveness is the generated thrust over input power. Despite this absence in the literature, it is our belief that the effectiveness is an important design factor. Thus, the key goal of this study is to arrive at scaling laws for plasma actuator effectiveness as a function of the operating parameters.

First we want to develop an experimental system that allow us to study the plasma actuator effectiveness, using current-voltage characteristics and power measurements, thrust measurements and optical measurements. Preliminary experiments will then be to study the basics of the plasma actuator. Then, operating parameters such as applied voltage amplitudes and frequencies will be studied. Plasma actuator configurations such as electrodes gap distance, electrode shape, electrode size, and dielectric thicknesses, will also be studied by optimizing the plasma performance. Then the research data will be analyzed to suggest possible methods for improving the performance of the plasma actuators, as well as potential scaling laws for actuator performance. We expect such scaling laws to be of great value in the design of more effective plasma actuators for flow control in low-pressure turbines.

Chapter 2. Experimental Apparatus

2.1 Overall experimetal setup

The whole plasma actuator is housed in a chamber that has a controlled atmosphere. The main adventage of using the gas chamber is it allow us to separate any surounding airflow from our plasma actuator. Since the generated thrust from our plasma actuator is approximately 1mN/m, elimating wind disturbance in our thrust measurements is essential. It also allowed us to test the plasma actuator with different ambient conditions, such as replacing the air with a helium ambient. A diagram of the chamber is shown in Figure 2.1a. A industeral grade helium gas tank is connected to the gas chamber, separated by a valve and a rotary vane vacuum pump (Trivac D8A) that allows the pressure to be controlled, along with a pressure gauge to moniter the pressure. When testing with helium gas, the chamber is evacuated approximately 10 minutes before each experiment, and then filled back to atmospheric pressure with helium gas. The gas chamber also allows electrical feed-through for power input and measurements, and is accessible for thrust and optical measurements. To power the plasma actuator, a function generator (Tektronix CFG253) is used, which generates various waveforms. Throughout the experiments presented in this report, only sinusoidal waveforms are used. This signal is then amplified by a power amplifier (Trek 20/20B) to a voltage of as high as 20kV peak-to-peak amplitude maximum, and with a current limitation of 20mA peak AC.

The experimental setup was easily modified for the effectiveness testing in atmospheric air, as shown in Figure 2.1b. A current-voltage characteristics and power measurement system are implemented to obtain the information for the effectiveness study. Since the main objective of the plasma actuator is to transfer momentum to the environment, it would be helpful to observe the generated thrust under various operating conditions. As shown in Figure 2.1b, the gas chamber is modified for thrust measurement. Although an opening is required for

the thrust measurement, flow disturbance is not large enough to affect the measurement. Also, an optical measurement system was implemented to provide information about the discharge structure. The discharge structure information the thrust measurement, and the current-voltage-power measurements, together lead to a better understanding of the plasma actuator fundamentals.

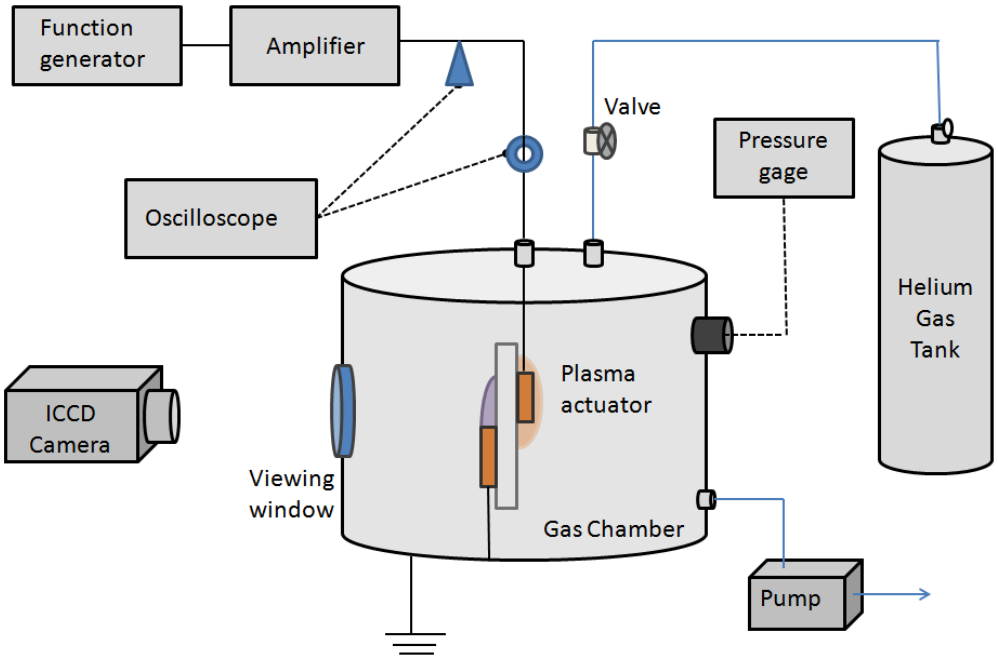

Figure 2.1a: Experimental setup with closed chamber for measurements in helium

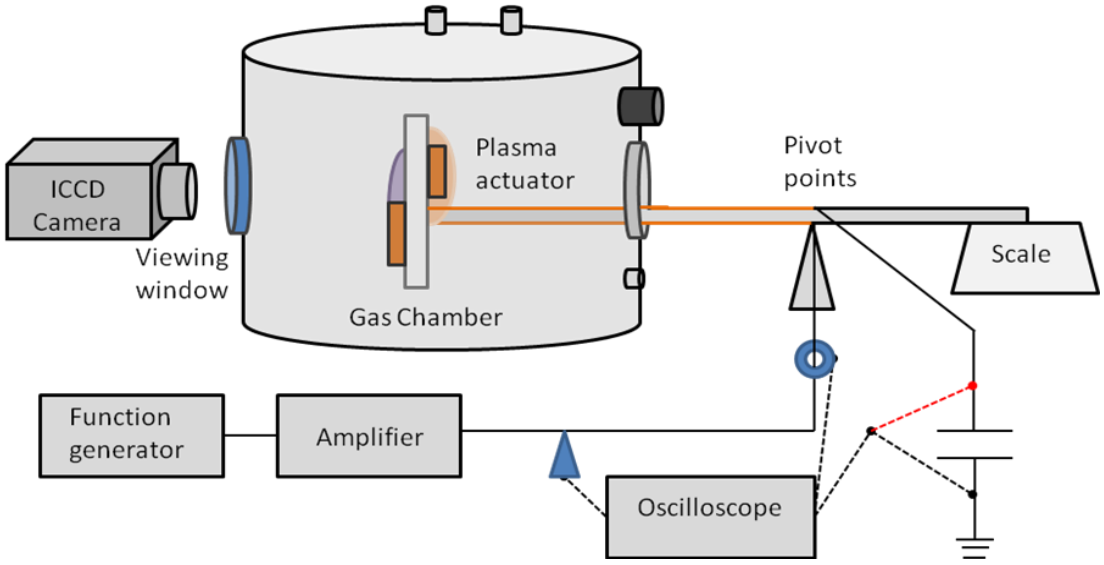

Figure 2.1b: Experimetal setup for effecitiveness measurements in atmosperhic air

2.2 Current-voltage characteristics and power measurement

The basic experimental setup for measuring the current-voltage (I-V) characteristics and power is shown in Figure 2.2. During the experiment, the input voltage was measured using a high voltage probe (Tektronix P6015A) located at the output of the amplifier. During initial studies, the discharge current was obtained by measuring the voltage drop across a sampling resistor (100 Ω) using an oscilloscope. This method was later replaced by monitoring the current with a current transformer (Pearson Current Monitor 6585), since it simplifies the measurements. Both the high voltage probe and the current transformer were connected to an oscilloscope (Tektronix TDS 460A) and the I-V waveforms were recorded. A typical I-V characteristic curve is shown in Figure 2.3.

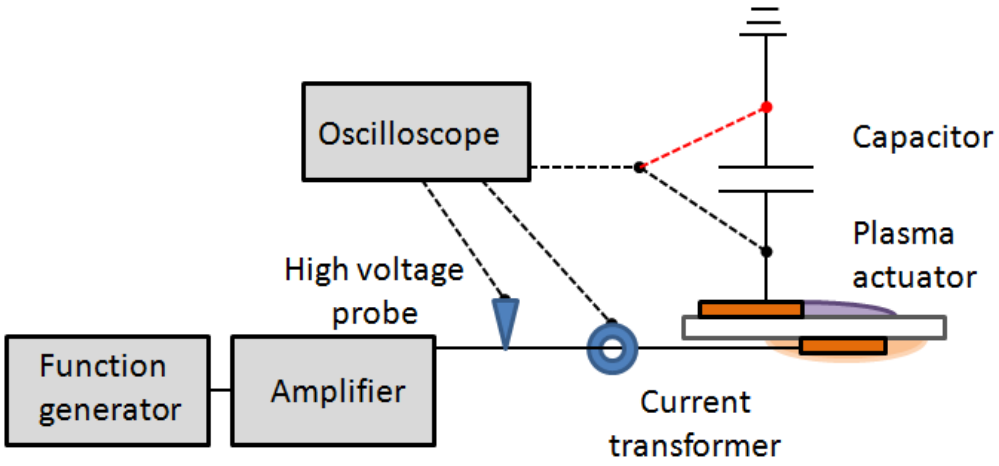

Figure 2.2: Schematic view of current-voltage characteristic and power measurement testing setup

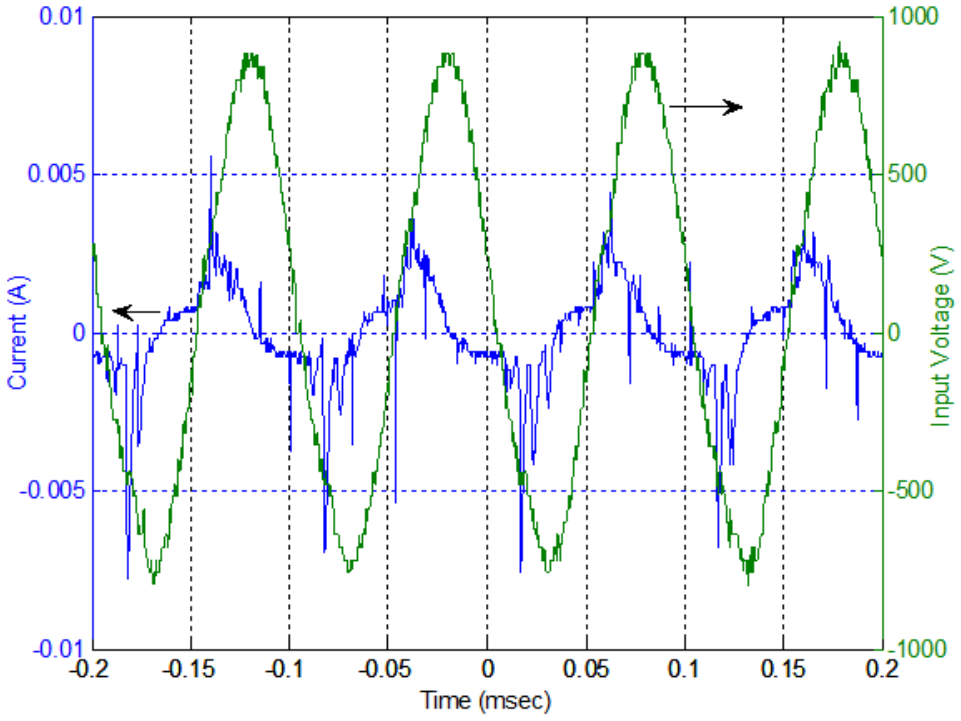

Figure 2.3: I-V curve for V_{in} = 0.8 kV amplitude at frequency 10kHz; helium at 760 Torr

In order to observe the time averaged power dissipated by the actuator, a 0.1μF capacitor was inserted between the non-powered electrode and ground. By measuring the voltage across this capacitor with respect to the applied voltage in the absence of a discharge, the actuator's off-state capacitance can be determined. In the presence of a discharge, measurement of the voltage across this capacitor as a function of applied voltage during an rf cycle can generate a plot of capacitor charge versus applied voltage. A typical plot is shown in Figure 2.4. From this plot, the power input to the actuator is determined by integrating the enclosed area. Pons et al. has a more detailed discussion on this power measurement method [20]. As the figure shows, some noise is observed during the experiment. The power measurement is considered to have an uncertainty of ±1W/m.

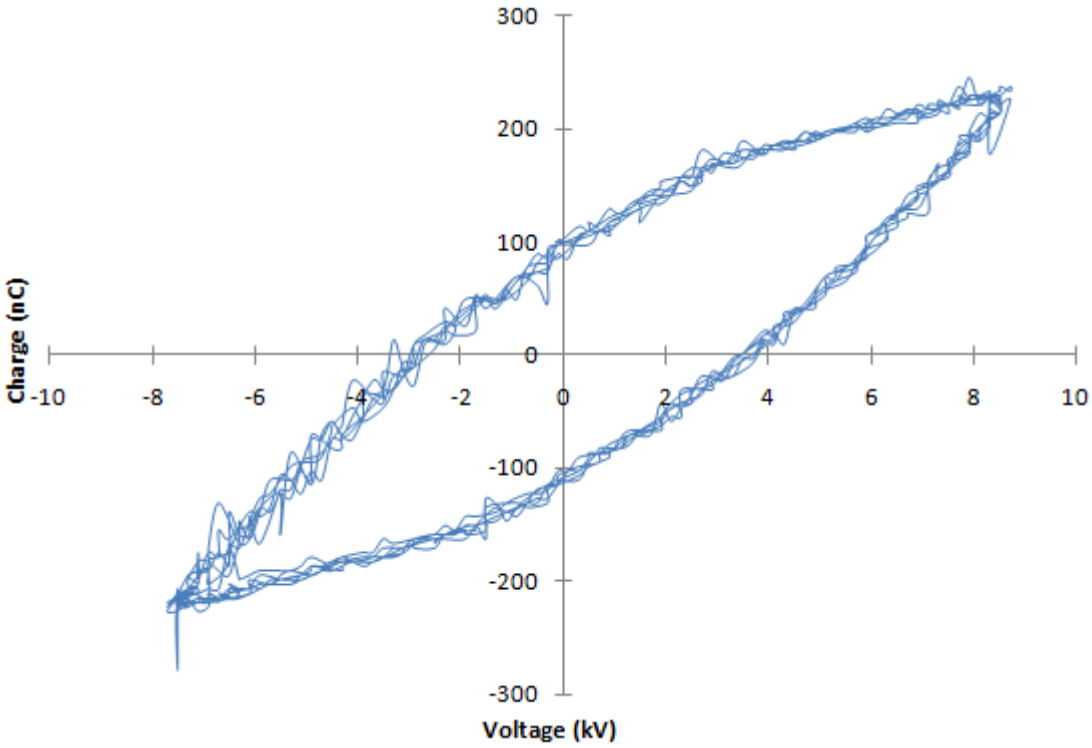

Figure 2.4: Charge on capacitor vs. applied voltage, $V_{in(p-p)}$ = 16 kV; frequency = 6kHz

2.3 Thrust measurement

The first of two thrust measurement systems consists of a pendulum mechanism. This pendulum system consists of a copper holder for delivering the AC power to the plasma actuator, as shown in the Figure 2.5. The copper holder not only acts as a supporter for the plasma actuator, but is also the electric feed-through to power the plasma actuator. With this design, the plasma actuator can move freely without any wires attached to it. Even a small amount of friction will affect the measurement due to the relatively small thrust generated by the plasma actuator. A small mirror is mounted to the front of the actuator. A laser beam is reflected onto a wall by the mirror. The thrust generated by the plasma discharge causes a deflection of the pendulum system which can then be calculated from the displacement of the laser beam image on the wall. However, this thrust measurement technique was difficult to use reliably in practice. With this pendulum mechanism, a relatively large fluctuation was observed during the recording of the experimental data, causing this setup to have approximately ±1 mN/m uncertainty. The major issue is that the holder (shown in figure 2.5 deforms after a period of time, thus causing inaccurate measurement data. Since the holder is made with thin copper, it is possible that it is not strong enough to support the plasma actuator, which causes the deformation. A second thrust measurement system was designed to overcome the problems with the pendulum technique.

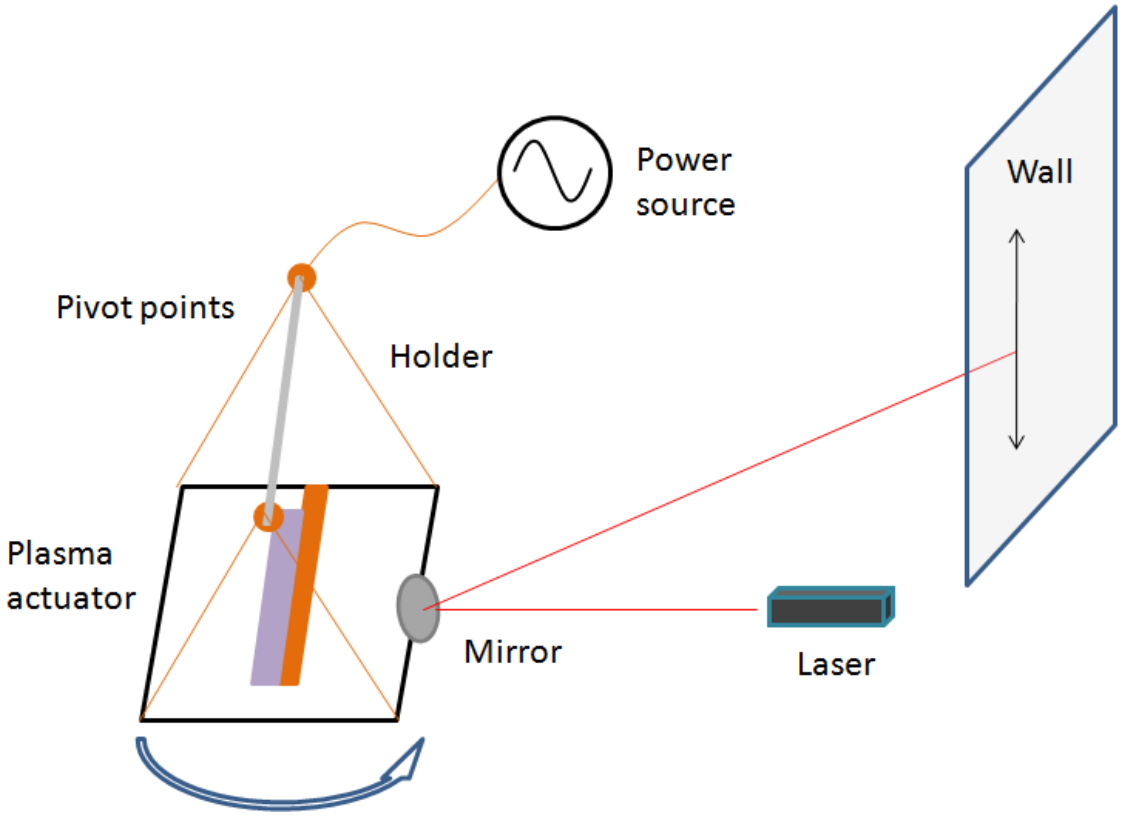

Figure 2.5: Schematic view of pendulum thrust measurement testing setup

The second thrust measurement technique included a lever system and an electric scale, as shown in Figure 2.6. This method is similar to the method used by Hoskinson et al. [21], with slight modification. Just like the pendulum system, the electronic feed-through was connected through the pivot point, thus preventing friction affecting the measurements. One side of the lever was attached to the plasma actuator, the other side was an electrical scale (AND GF-300). The thrust generated by the plasma discharge was determined by the change of the measured weight on the scale, *Wd*, for the plasma "on" versus plasma "off" conditions. Then, knowing lengths *A* and *B*, and the standard gravity *g*, the thrust can be determined from the equation: $T=Wd \times g \times A/B$. The thrust per unit length generated by the plasma actuator is then found by dividing the thrust by the width of the plasma actuator. Due to the lever system design, the measurement reading fluctuates, causing the measurement to have

approximately ±0.5mN/m uncertainty. The accuracy is better than the pendulum design, however. This experimental setup also has a high repeatability, since the setup is more stable.

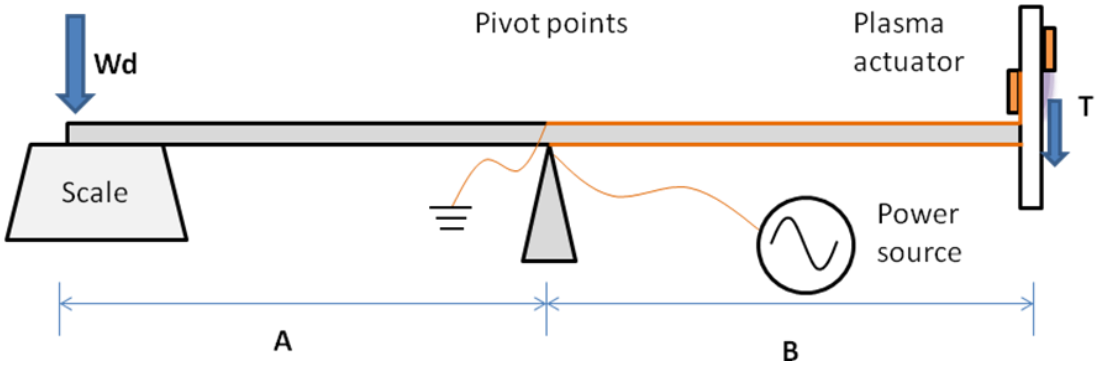

Figure 2.6: Schematic view of lever thrust measurement testing setup

2.4 Optical measurement

For optical measurements, we used an intensified charge-coupled device (ICCD) camera (Princeton Instruments: PI-MAX). The experimental set up is shown in Figure 2.7. The ICCD camera was connected to a shutter trigger box, which controls the ICCD camera's shutter. The trigger box is connected to a pulse generator, which generates the trigger signal for the system. When a picture is taken, the data are sent to a computer for processing by Princeton instruments spectroscopic software, WinSpec/32.

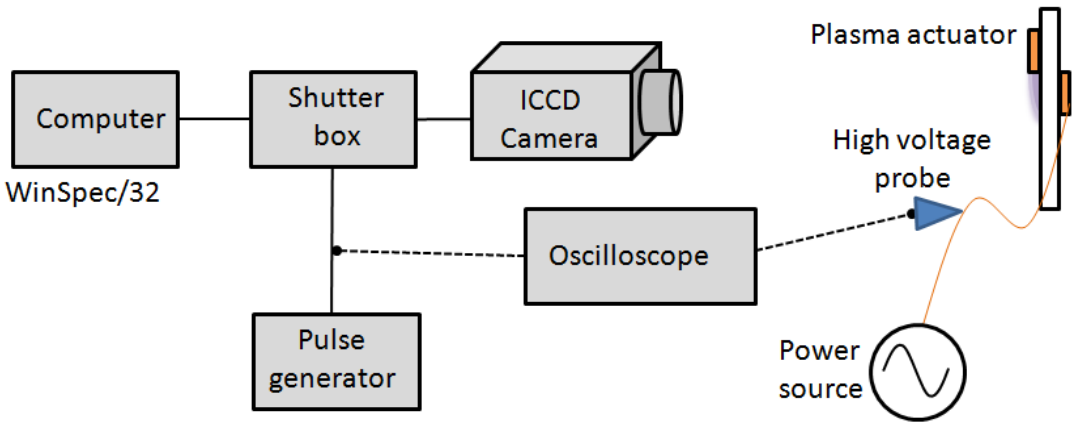

Figure 2.7: Schematic view of optical measurement testing setup

In a typical setting, the pulse generator (Systron Donner 101) provides a pulse which triggers both the PI-MAX ICCD camera's shutter to take the picture and the oscilloscope to record the applied voltage and the current signals. The timing scheme for the experiment is shown in Figure 2.8a. The ICCD camera was set to an exposure time of 10μs. The oscilloscope recorded for 0.5ms before and after the trigger pulse. Therefore, the voltage and current signals were observed over a total of 1ms for each image.

In some occasions, it was desirable to observe the plasma actuator for a full half cycle. In order to do so, the pulse generator is not required. Instead, internal pulses generated from the function generator were used to directly trigger the ICCD camera. Those pulses were synchronized with the applied voltage sine wave, as shown in Figure 2.8b. In this configuration, it was possible to control the camera to record images of individual cycles of the plasma actuator, by setting the camera expose time to the half cycle of the sine wave. During positive current mode, the photo-cathode is active during the negative pulse, whereas during the negative current mode, the photo-cathode is active during the positive pulse. This allows us to compare the plasma during the rising or falling half cycle. This will be further explained in the experimental section when the experiential.

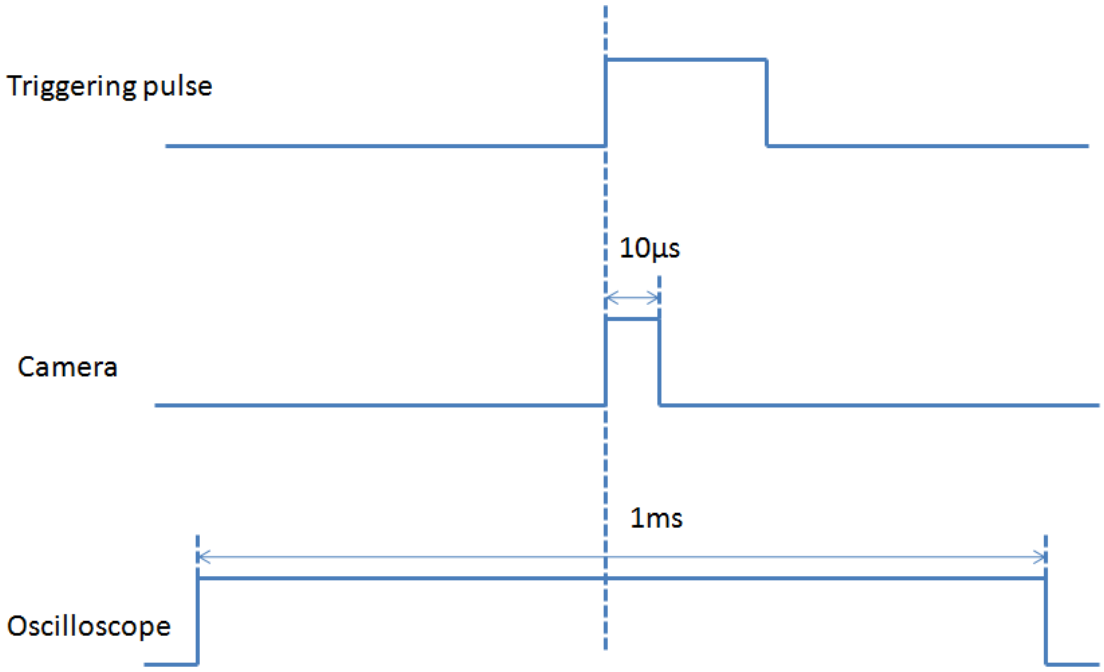

Figure 2.8a: Timing of optical experiment with pulse generator

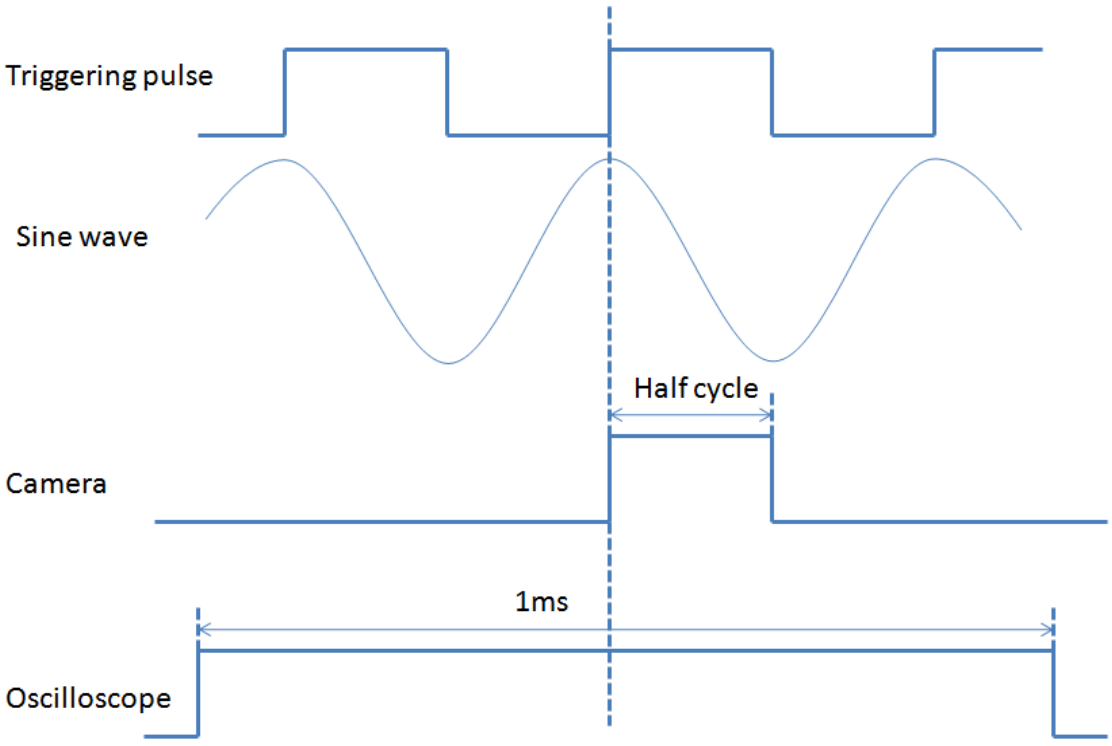

Figure 2-8b: Timing of optical experiment with function generator

Chapter 3. Preliminary Experiment

3.1 Preliminary experiment in helium

Initial experiments focused on helium since this is a particularly well studied and understood system [22]. The initial plasma actuator design was constructed using copper tape electrodes and an aluminum oxide sheet for the dielectric, as shown in Figure 3.1. The copper tape was 0.089 mm (0.0035 inch) thick and 6.35 mm (0.25 inch) wide. The aluminum oxide sheet was 0.635 mm (0.025 inch) thick. The covered electrode was covered with polyimide (Kapton) tape to prevent a discharge on that side of the actuator. There was a 1 mm overlap between the trailing edge of the exposed electrode and the leading edge of the covered electrode.

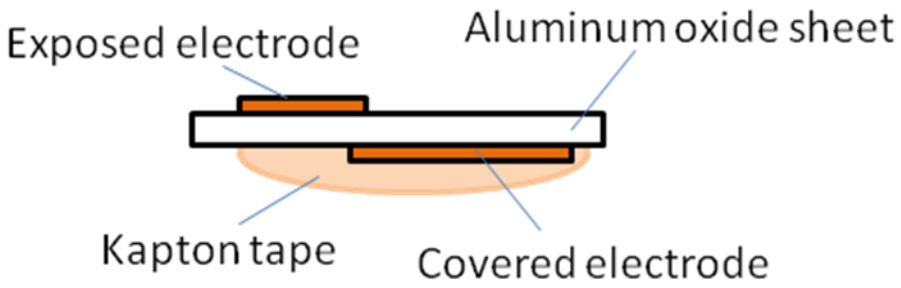

Figure 3.1: Schematic of plasma actuator setup

3.1.1 Current-Voltage characteristics measurements

Figure 3.2 shows the applied voltage and current under the following conditions: helium atmosphere at 760 Torr and applied voltage of 1.6 kV amplitude peak-to-peak at 10kHz. As shown in this figure, the current signal has two components: a capacitive sinusoidal component and an overlying component due to the discharge current. As expected, the capacitive (displacement) current is 90 degrees out of phase with the applied voltage. It is obvious that the discharge current component is asymmetric between the positive and negative current half-

cycles. According to the electrical setup, a positive current signifies a current flowing toward the exposed electrode, as shown in figure 3.3.

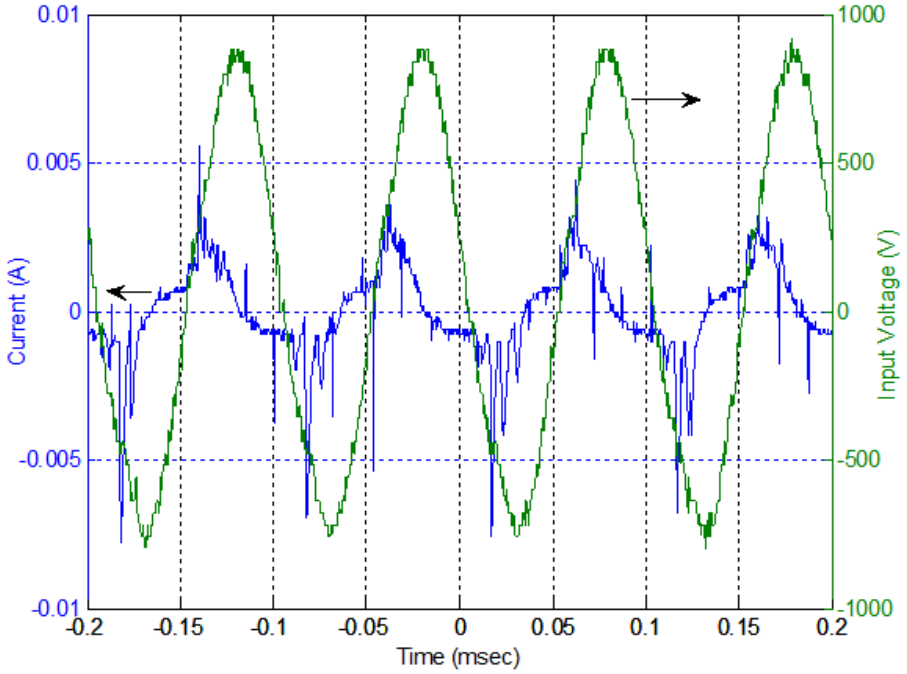

Figure 3.2: Discharge current versus applied voltage

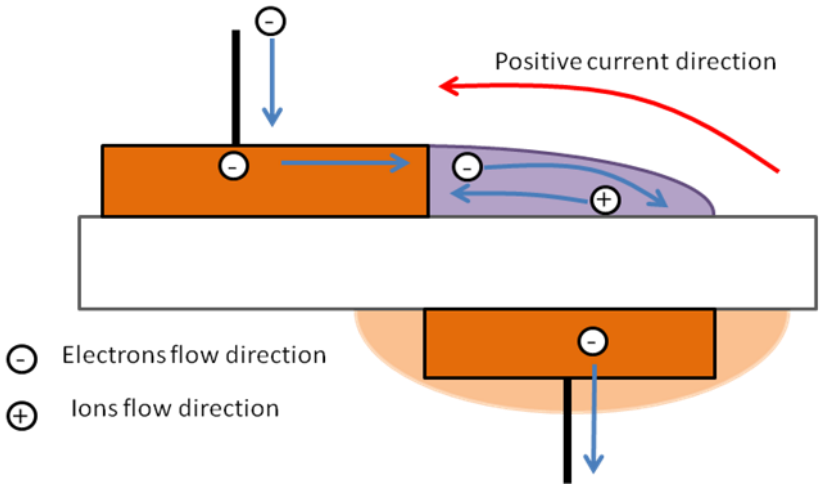

Figure 3.3: Electron and ion flow directions during positive current half cycle

- **Current characteristics for different input frequencies**

Measurements were conducted over a range of input frequencies at a fixed applied voltage to determine the effect of input frequency on the current characteristics. The results of these measurements, for fixed applied voltage peak-to-peak amplitude of 2 kV, are shown in Figure 3.4. The amplitude of the discharge current is seen to increase with increasing input frequency. This is as expected since the current limiting effect of the dielectric's AC impedance decreases with increasing frequency. The frequency also affects the number of peaks in the negative current cycle, suggesting that fewer, more energetic breakdowns occur at higher frequencies.

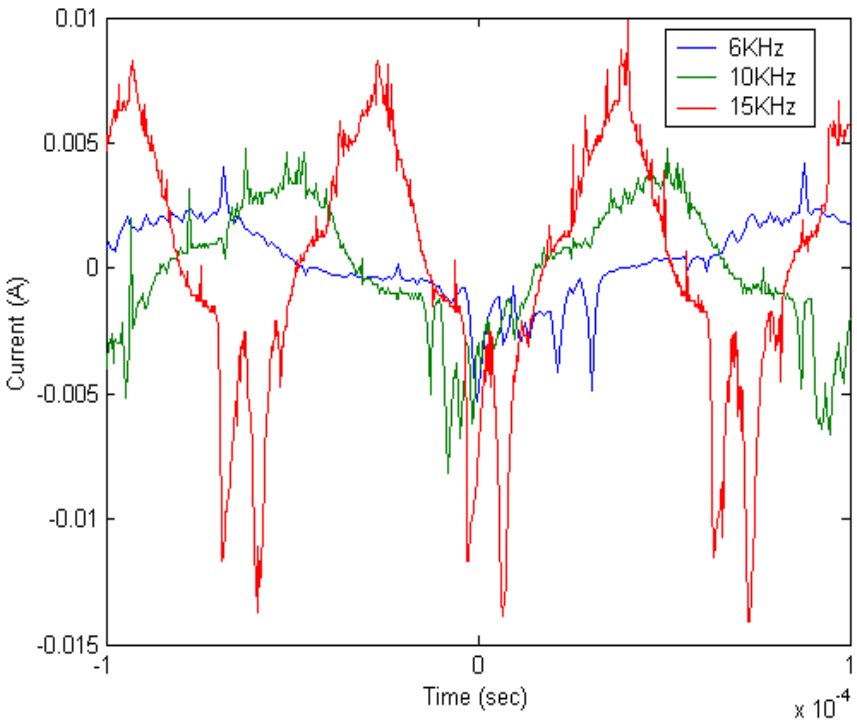

Figure 3.4: Comparison of current for different input frequencies, $V_{in(p-p)}$ = 2kV

- **Current characteristics for different applied voltages**

Measurement were also conducted over a range applied voltages at a fixed frequency to determine the effect of applied voltage on the current characteristics, as shown in Figure 3.5 for a fixed frequency or 10 kHz. Figure 3.5 shows that the amplitude of the current also increases with increasing applied voltage amplitude. It should be noted that peak-to-peak amplitude of 2.4 kV is just below the voltage at which uncontrolled arcing occurs at the electrode terminals. The graph also shows that discharge breakdown happens earlier in the cycle with a higher voltage. This is not surprising, since a higher amplitude leads to an earlier breakdown.

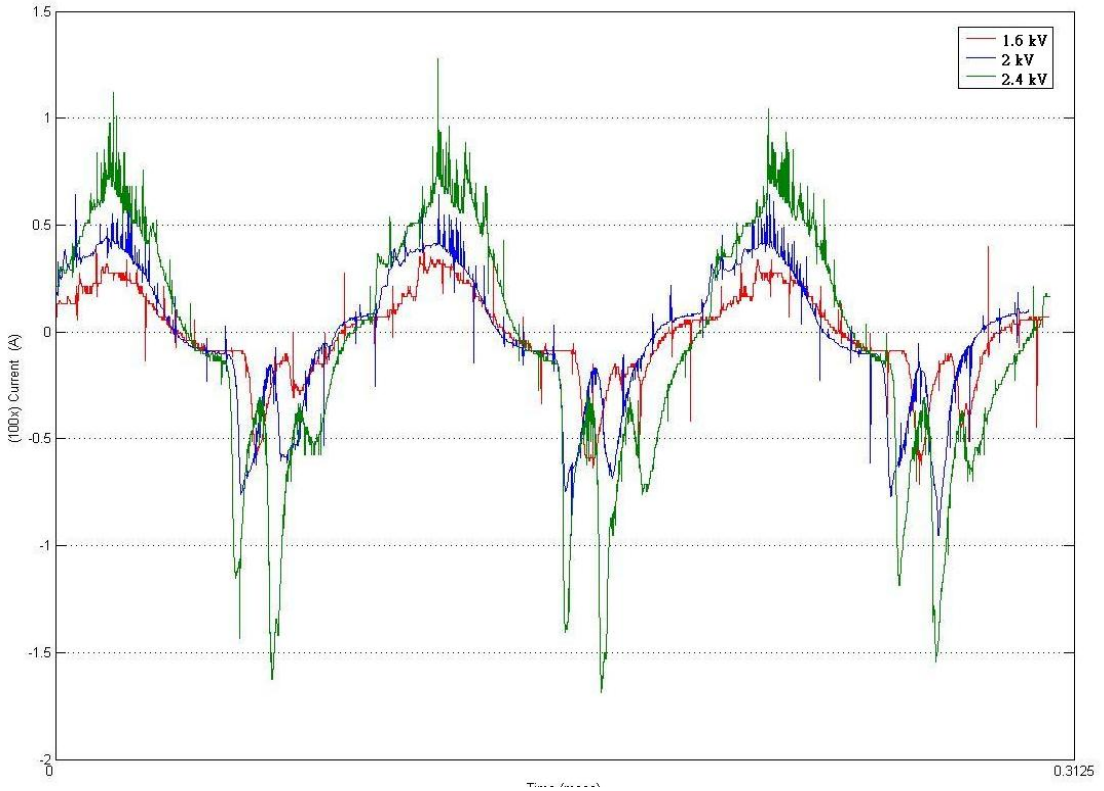

Figure 3.5: Comparison of current for different applied voltages; frequency = 10kHz

3.1.2 Optical measurements

In order to investigate the asymmetric discharge structures during the positive and negative current half cycles apparent in Figure 3.2, images of the plasma emission were taken with the ICCD camera together with current and voltage measurements. Figure 3.6 shows a comparison between the two opposite current half cycles for a plasma actuator operated at a frequency of 10 kHz with a peak-to-peak amplitude of 2.4 kV.

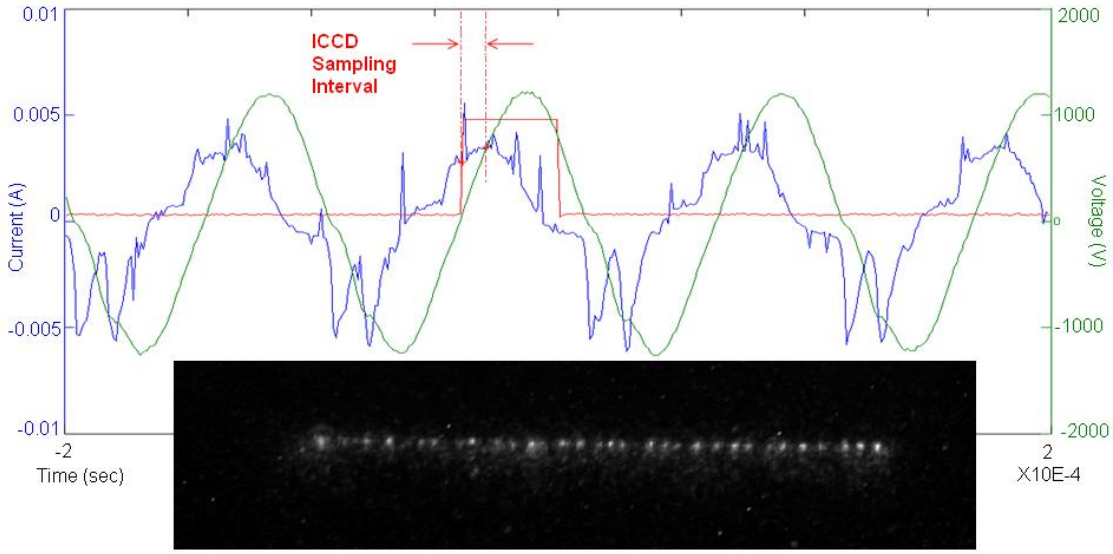

Figure 3.6a: Discharge structure during positive current half cycle

$V_{in(p\text{-}p)}$ = 2.4 kV; frequency = 10 kHz; helium at 760 Torr

Photo is taken during the period marked by the arrows indicating the ICCD sampling interval.

Figure 3.6a, taken during the positive current half cycle, clearly shows a set of filaments in the lateral direction along the plasma actuator. While the current appears to have one broad peak with superimposed spikes, we believe that this was an artifact of the experimental setup. Filamentary micro-discharges typically

have lifetimes of 1-20 ns [6]. This is at the limit of the time-resolution of the equipment used, making a fast sequence of short spikes appear like one broad current pulse.

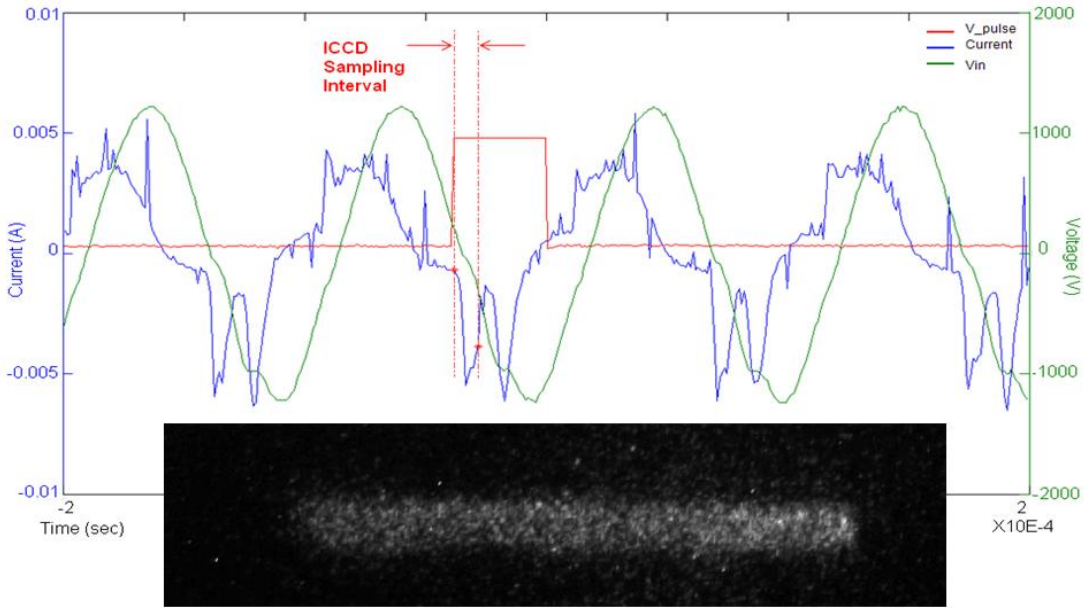

Figure 3.6b: Discharge structure during negative current half cycle

$V_{in(p-p)}$ = 2.4 kV; frequency = 10 kHz; helium at 760 Torr

During the negative current half cycle, two large, broad current peaks are observed. The time-scale of these peaks is of the order of a few µs, which is consistent with the time-scales of a uniform atmospheric pressure glow discharge pulse [23]. Indeed, Figure 3.6b demonstrates that plasma is significantly more uniform, i. e., glow-like discharge during this part of the cycle.

A series of images were also taken under the same conditions as for Figure 3.6, but with a lower frequency of 6 kHz. The results are shown in Figure 3.7.

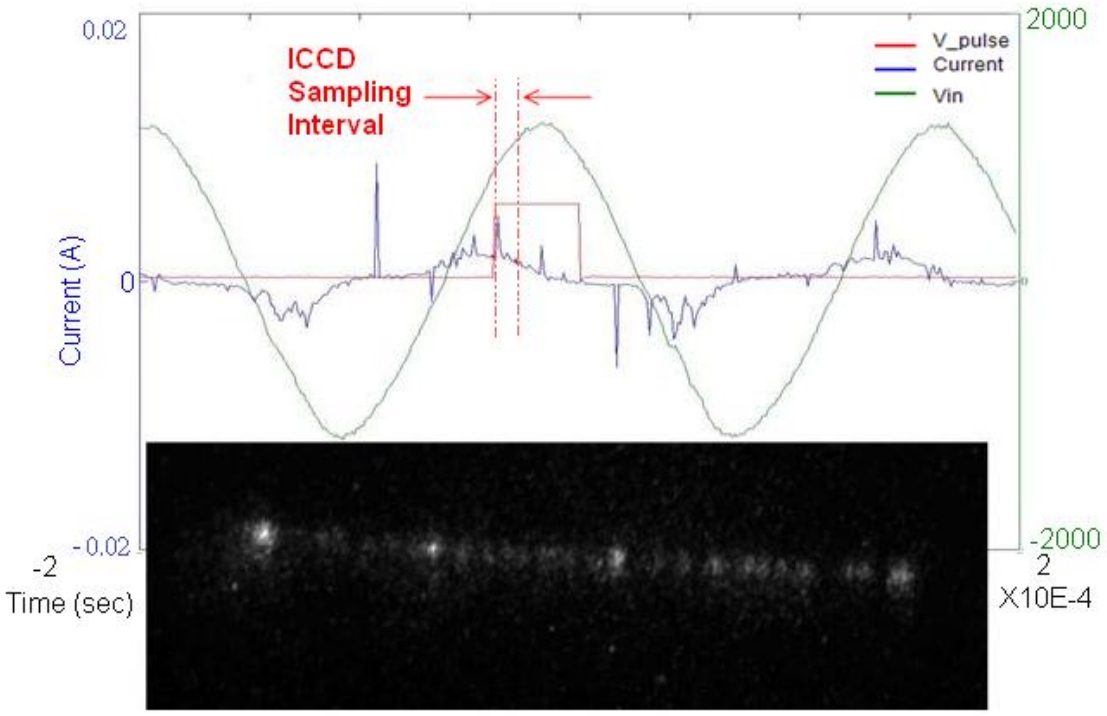

Figure 3.7a: Discharge structure during positive current half cycle

$V_{in(p-p)}$ = 2.4 kV; frequency = 6 kHz; helium at 760 Torr

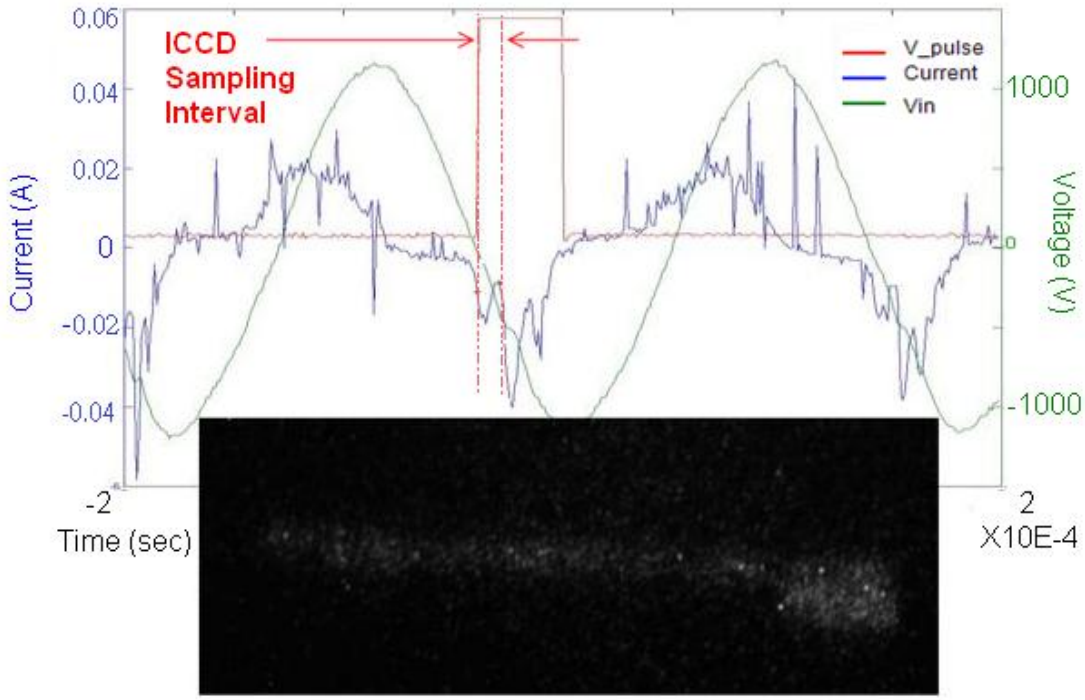

Figure 3.7b: Discharge structure during negative current half cycle

$V_{in(p-p)}$ = 2.4 kV; frequency = 6 kHz; helium at 760 Torr

Two observations can be made compared to the 10 kHz case: (A) the luminosity of the plasma is lower at lower frequency and (B) filaments are still observed during positive current cycles, however the plasma is not as uniform during the negative current half cycle. The lower luminosity at lower frequency results from an increase of the impedance of the dielectric barrier structure when operating at lower frequency. This leads to a smaller voltage drop across the plasma and a less intense discharge.

Finally, a series of images were taken under the same conditions as Figures 3.6 and 3.7, except for a higher frequency of 15 kHz. These results are shown in Figure 3.8.

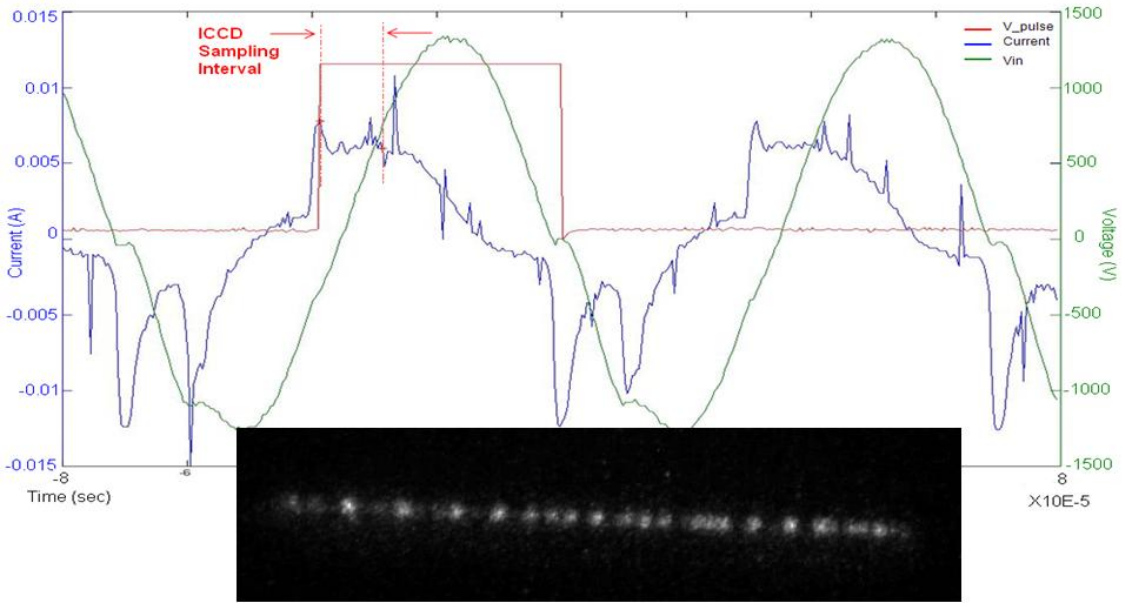

Figure 3.8a: Discharge structure during positive current half cycle

$V_{in(p-p)}$ = 2.4 kV; frequency = 15 kHz; helium at 760 Torr

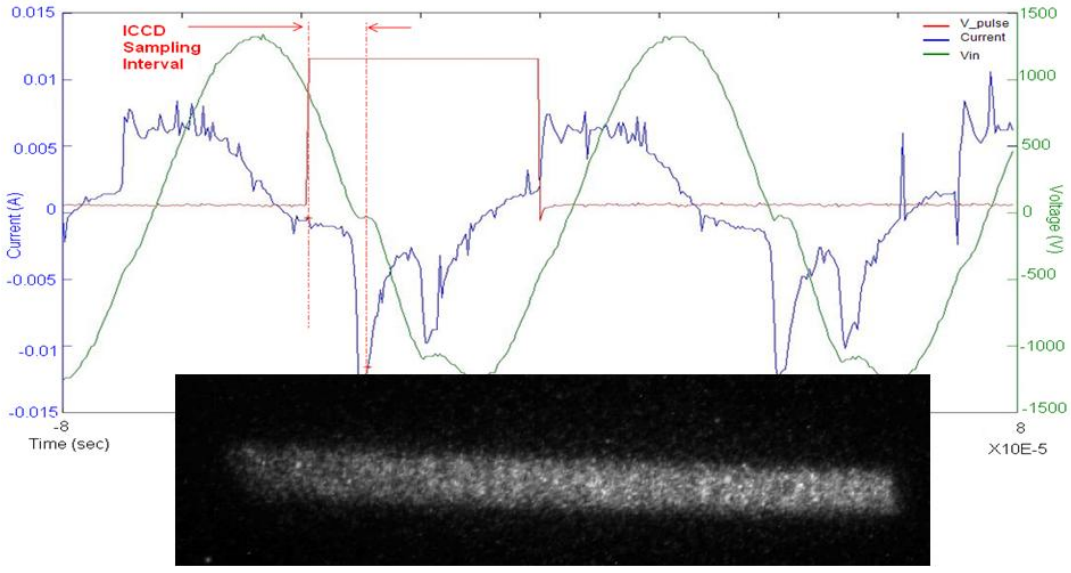

Figure 3.8b. Discharge structure during negative current half cycle

$V_{in(p-p)}$ = 2.4 kV; frequency = 15 kHz; helium at 760 Torr

Compared to the 10 kHz and 6 kHz cases, the luminosity increased and the two broad peaks during the negative half cycle were more clearly defined. These

observations are related to the decreased impedance of the dielectric barrier structure at higher frequencies, leading to a higher voltage drop across the plasma and a more intense discharge.

3.2 Preliminary experiment in air

Preliminary measurements of plasma actuator characteristics were also conducted in a more realistic air chemistry environment: atmospheric pressure air. Under these conditions, the thrust of the plasma actuator was measured verses various applied voltage conditions using the pendulum thrust measurement system. Current, voltage and optical measurements were also taken for comparison with the experiments in helium.

3.2.1 Thrust measurements

The thrust was measured in 1 atmospheric pressure air as a function of the magnitude of applied voltage for two different frequencies. The results are shown in Figure 3.9.

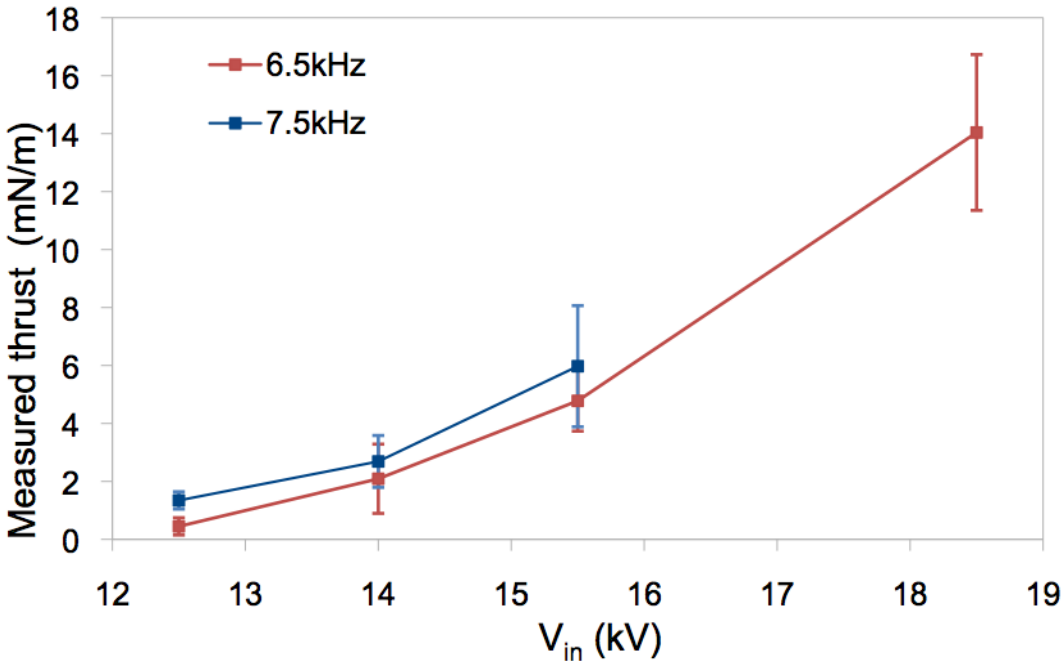

Figure 3.9: Thrust versus applied voltage peak-to-peak amplitude with different frequencies

The results show that the thrust increases with both increasing applied voltage amplitude and increasing frequency. With an increase in voltage amplitude, the higher voltage occurring across the plasma leads to a more intense discharge and thus higher observed thrust. Similarly, due to the decrease in impedance of the dielectric barrier structure with increasing frequency, an increase in frequency also leads to a higher voltage across the plasma and thus a more intense discharge and higher thrust.

3.2.2 Current-voltage characteristics and optical measurements

While for the experiments conducted in helium, the thrust could not be measured due to the resolution limit of the pendulum system, a comparison of current-voltage characteristics and ICCD images between operation of the plasma actuator in helium and air was possible. Results for plasma actuator operation in 1 atmosphere air for an applied voltage of 15 kV peak-to-peak and a frequency of 8.5 kHz are shown in Figures 3.10. Note from a comparison with Figures 3.6, that the applied voltage amplitude is much higher in air than it was in helium. This results from the higher breakdown voltage of air versus helium. In addition, the current waveform is shaped differently between the air and the helium cases, with the air discharge having more spikes during the negative half cycle. The images are taken during the 10 μsec time interval indicated by the pulse.

During the positive current half cycle, shown in Figure 3.10a, the electrons are traveling away from the exposed electrode. The plasma actuator then generates a more streamer-like discharge during this half cycle. The non-uniformity of the exposed electrode could be one of the reasons for this observed non-uniformity of the plasma. In comparing this image with the images taken at a pressure of one atmospheric in helium, similar characteristics are observed. However, the streamer-like discharge extends farther from the exposed electrode in air, compared with its extent in helium, as shown in Figure 3.6a.

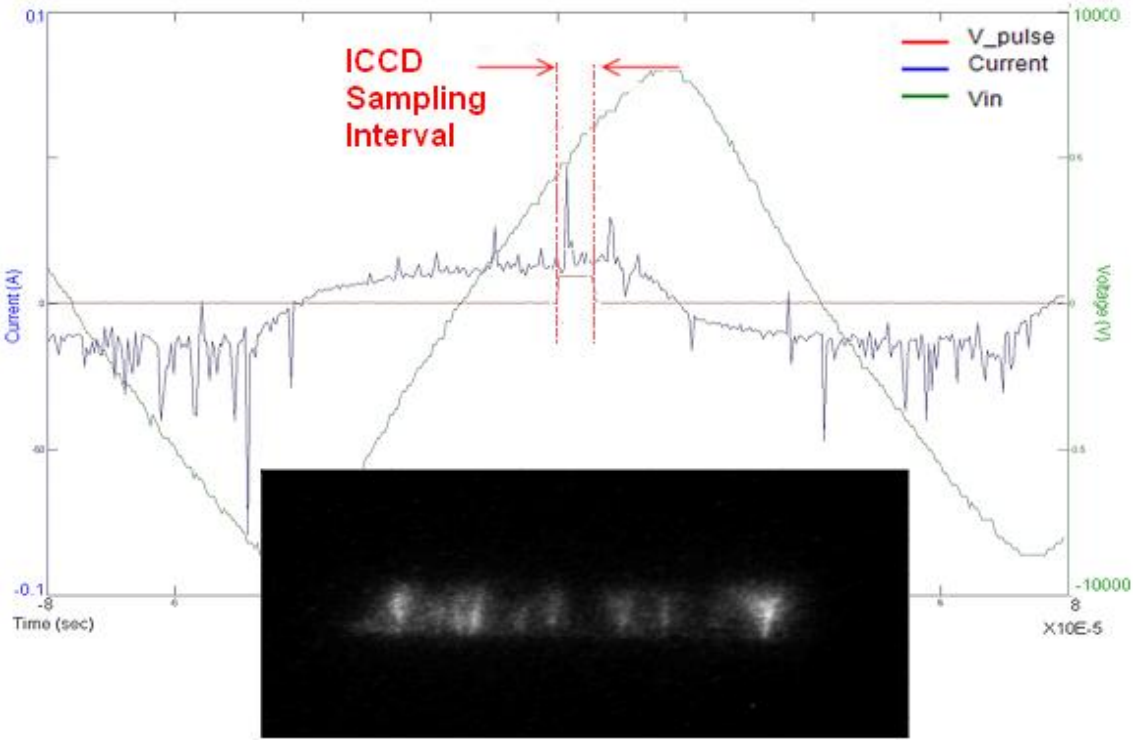

Figure 3.10a: Discharge structure during positive current half cycle in air

$V_{in(p\text{-}p)}$ = 15 kV; frequency = 8.5 kHz; air at 760 Torr

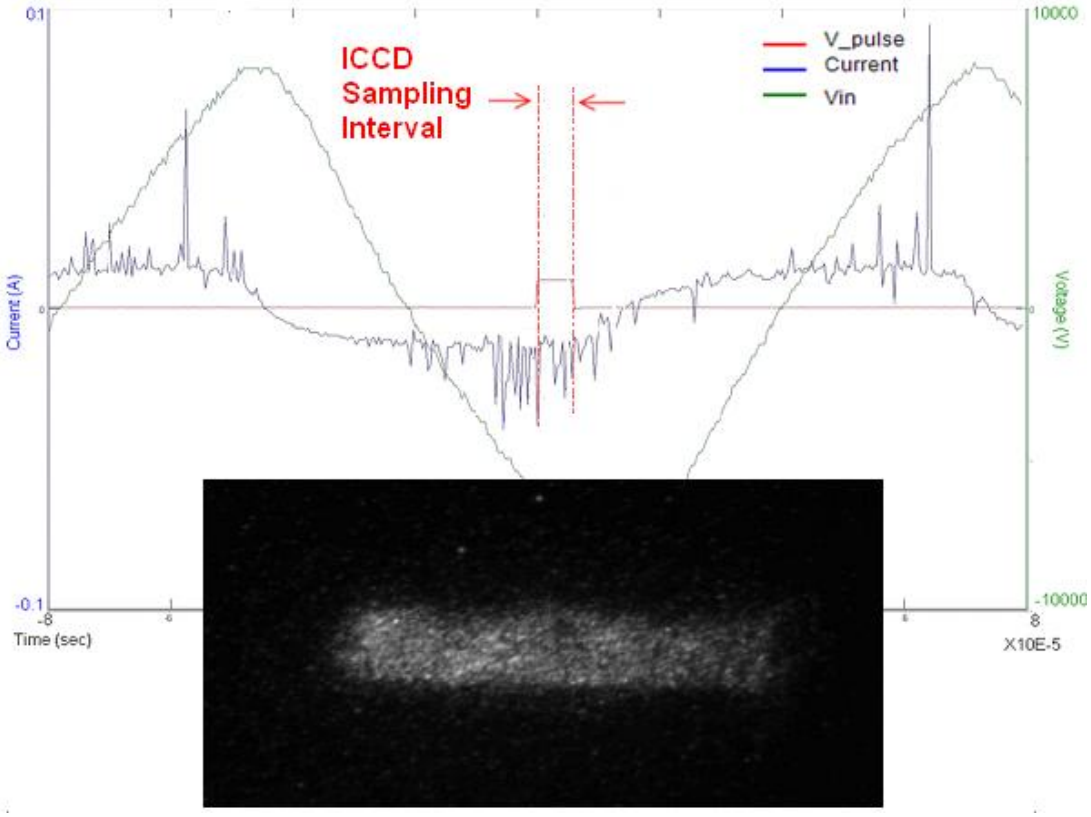

Figure 3.10b: Discharge structure during negative current half cycle in air

$V_{in(p-p)}$ = 15 kV; frequency = 8.5 kHz; air at 760 Torr

The image in Figure 3.10b shows that during the negative current half cycle, when electrons are going from the dielectric to the exposed electrode, a relatively uniform plasma discharge is generated by the plasma actuator. Similar characteristics are observed when comparing to the image taken in helium at one atmosphere pressure, Figure 3.6b.

3.2.3 Generated thrust versus electrode gap distance

As part of these preliminary experiments in 1 atmosphere air, the effect of actuator geometry on operating characteristics was also studied. We investigated the effect of the actuator's gap size (the stream-wise distance between the upper

exposed electrode's trailing edge and the lower covered electrode's leading edge, as indicated in Figure 3.11) on actuator performance. In these studies, the gap size was varied from a 2.0 mm gap to an overlap of 10.0mm. The actuator was constructed using a 0.63mm (0.025 inch) thick aluminum oxide sheet as the dielectric and the bottom electrode was covered with polyimide (Kapton) tape.

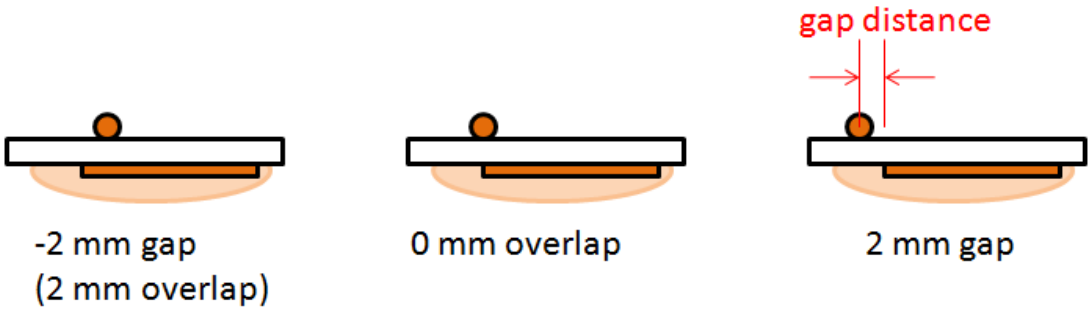

Figure 3.11: Configurations of plasma actuator geometries

A plot of thrust versus the overlap distance for a frequency of 6 kHz and applied voltage peak-to-peak amplitude of 16 kV is shown in Figure 3.12. The results show that the maximum thrust is measured when there is a small gap present between electrodes.

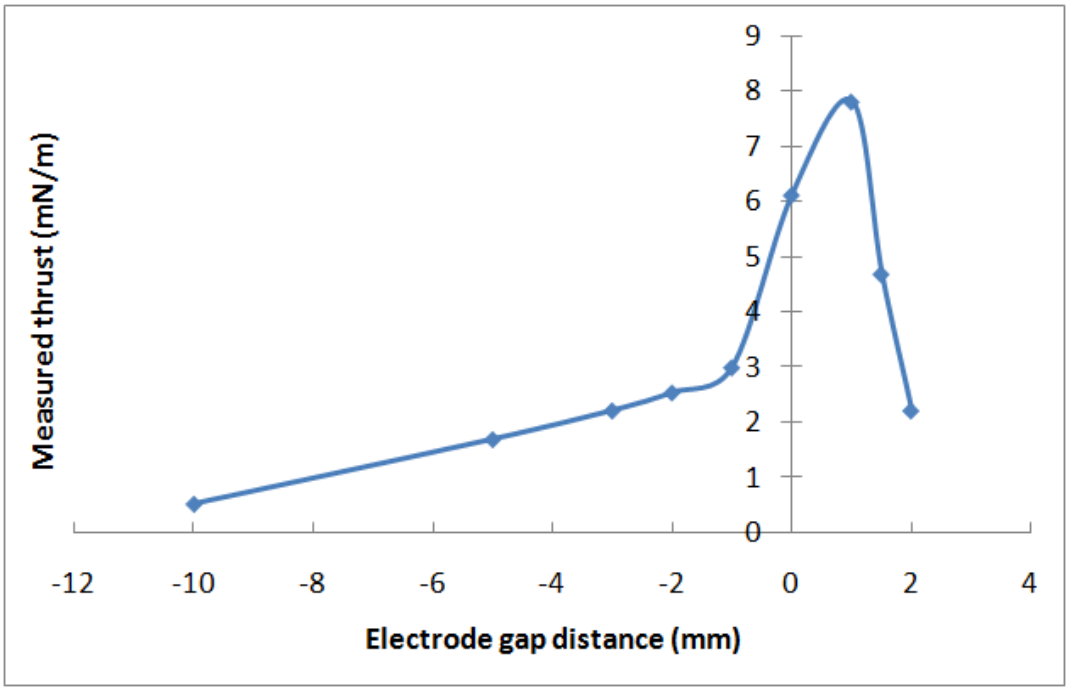

Figure 3.12: Thrust versus gap distance of the wire electrode for $V_{in(p-p)}$ = 16 kV and Frequency = 6kHz

The measurements shown in Figure 3.12 are consistent with results from Forte et al. [18], shown in Figure 3.13. In both studies, maximum thrust occurs for a small gap distance. These results show that the geometry of the plasma actuator indeed has an effect on the plasma actuator performance. A more detailed study on the plasma actuator geometry effect will be shown in the next section.

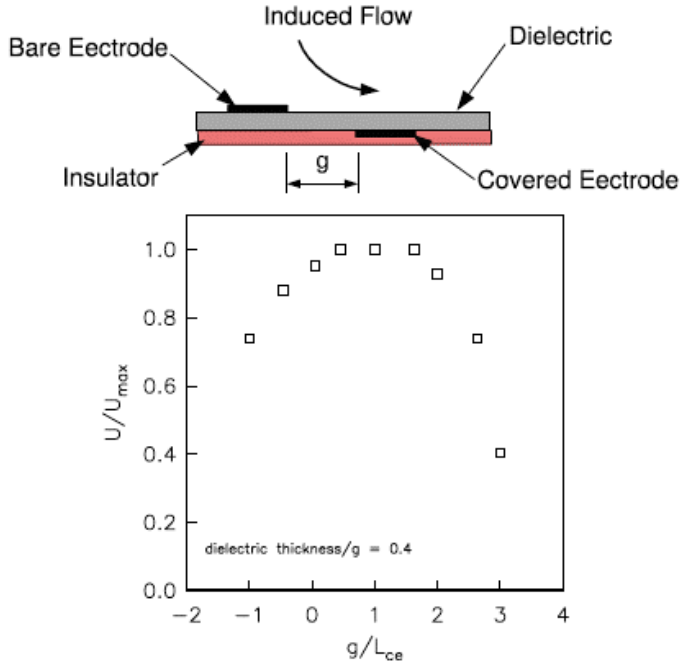

Figure 3.13: Effect of gap spacing between bare and covered electrodes on maximum induced velocity in still air [18]

3.3 Summary

This set of experiments demonstrated typical plasma current-voltage characteristics, showing that the plasma actuator DBD indeed consists of a collection of micro-discharge channels. The current-voltage characteristic measurements also suggest that the plasma structure is different between the negative current half cycle and the positive current half cycle. Through optical measurements, the asymmetric nature of the discharge structures between the positive and negative half cycles were demonstrated, confirming the asymmetry indicated in the current-voltage measurements. The experimental results from both air and helium are very similar, with air operation requiring a higher applied voltage and generating more spikes during the negative current half cycle. Thrust was also measured in air under various applied voltage and frequency conditions. An effect of plasma actuator geometry on thrust was also observed,

with maximum thrust occurring for a small gap between the trailing edge of the exposed electrode and the leading edge of the covered electrode.

Chapter 4. Main Experimental Results and Data Analysis

As mentioned earlier, the objective of this study is to arrive at scaling laws for plasma actuator effectiveness as a function of the operating parameters. One important and obvious parameter indicating plasma actuator effectiveness is the generated thrust. As shown in the preliminary experiments discussed in Chapter 3 and the literature, the thrust generated by a DBD plasma actuator is strongly dependent on the asymmetry of the plasma actuator [24]. Thus, the materials and geometry of the plasma actuator are main factors that can be manipulated to alter the thrust. By changing the electrode geometry and the dielectric sheet properties, e.g. composition and thickness, the asymmetry between the uniform and filamentary portions of the discharge cycle can be modified to increase thrust. Consequently we explored the performance of plasma actuators constructed using different electrode geometries and dielectric properties.

4.1 Effectiveness study

4.1.1 Plasma actuator effectiveness versus frequency

The first plasma actuator design used in this set of measurements was constructed using copper tape electrodes and an aluminum oxide sheet for the dielectric, as shown in Figure 4.1. The copper tape was 0.089 mm (0.0035 inch) thick and 6.35 mm (0.25 inch) wide. The aluminum oxide sheet was 0.635 mm (0.025 inch) thick. The covered electrode was covered with polyimide (Kapton) tape to prevent a discharge on that side of the actuator. There was a 1mm overlap between the trailing edge of the exposed electrode and the leading edge of the covered electrode.

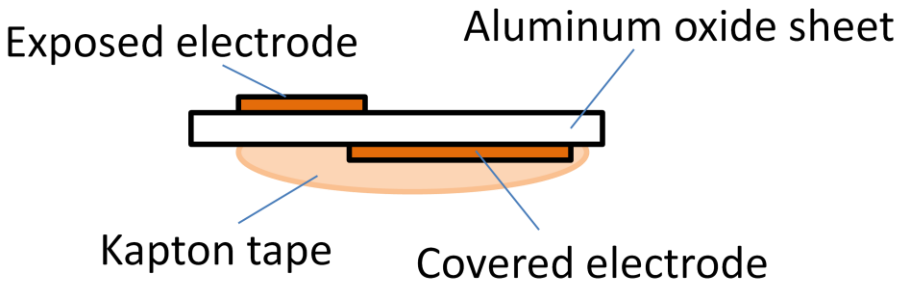

Figure 4.1: Schematic of plasma actuator setup

Figure 4.2 illustrates the effect of the frequency of the applied voltage on actuator effectiveness for this design. As mentioned earlier, we defined the plasma actuator effectiveness as the thrust generated from the plasma actuator divided by the power the plasma actuator consumed. In Figure 4.2, thrust is shown as a function of power for three applied voltages of 12kV, 14kV, and 16kV peak-to-peak amplitude and for three different frequencies of 5kHz, 6kHz, and 7kHz. Thus, the slope of the curve for a given frequency is the plasma actuator effectiveness for the frequency. From these results, it is seen that a lower driving frequency yields a higher effectiveness. i.e. the plasma actuator consumes less power at lower frequencies than at higher frequencies to achieve the same thrust. Since the frequency of the applied voltage various with the impedance of the dielectric barrier structure, this suggests that the impedance of the dielectric is could be an important factor of the plasma actuator effectiveness.

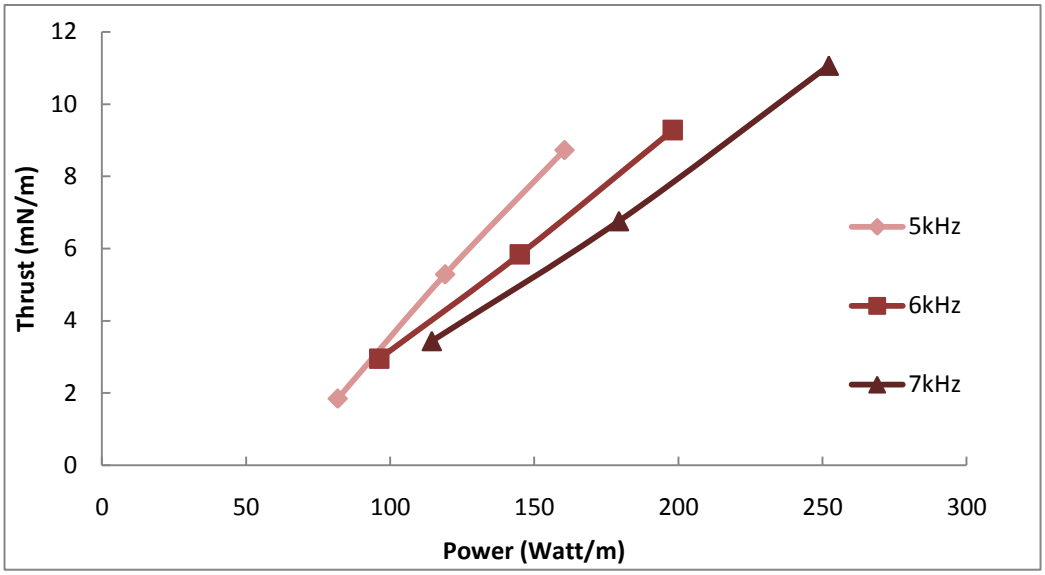

Figure 4.2: Thrust versus power input for various applied frequencies

4.1.2. Plasma actuator effectiveness versus electrode gap size

The effect of the electrode gap size (the stream-wise distance between the upper exposed electrode's trailing edge and the lower covered electrode's leading edge) on actuator performance was also investigated. In these studies, the gap size was varied from a 2.0 mm gap to an overlap of 1.0 mm, as shown in Figure 4.3. The actuator was constructed using a 0.63mm (0.025 inch) thick aluminum oxide sheet as the dielectric and the covered electrode (bottom electrode in Figure 4.3) was covered with polyimide (Kapton) tape.

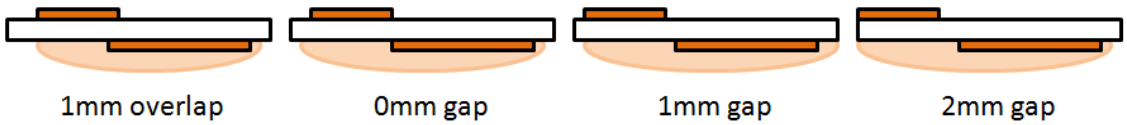

Figure 4.3: Schematic of plasma actuator setup for various electrode gap sizes

Figure 4.4 shows thrust versus input power measurements for various gap distances at a fixed frequency of 7 kHz for three applied voltages of 12kV, 14kV and 16kV peak-to-peak. These results indicate that as long as there is a gap between electrodes, plasma actuator effectiveness is relatively insensitive to gap

size. The plots show, however, that the power required to achieve a particular thrust is significantly higher when there is an overlap rather than when there is no overlap. Consequently, it appears that a small gap is preferred for better performance. These measurements are consistent with results from Forte et al. This could be because when a small gap is present between the electrodes, it prevents the ions from being deposited on the plane downstream but very close to the exposed electrode, forcing the ions to accelerate further downstream [18]. In both studies, best performance occurs for a small gap. However, when the electrode gap is too large, the maximum thrust achieved from the plasma actuator will decrease as well. This is likely due to the weakening of the electric filed causing a weaker plasma.

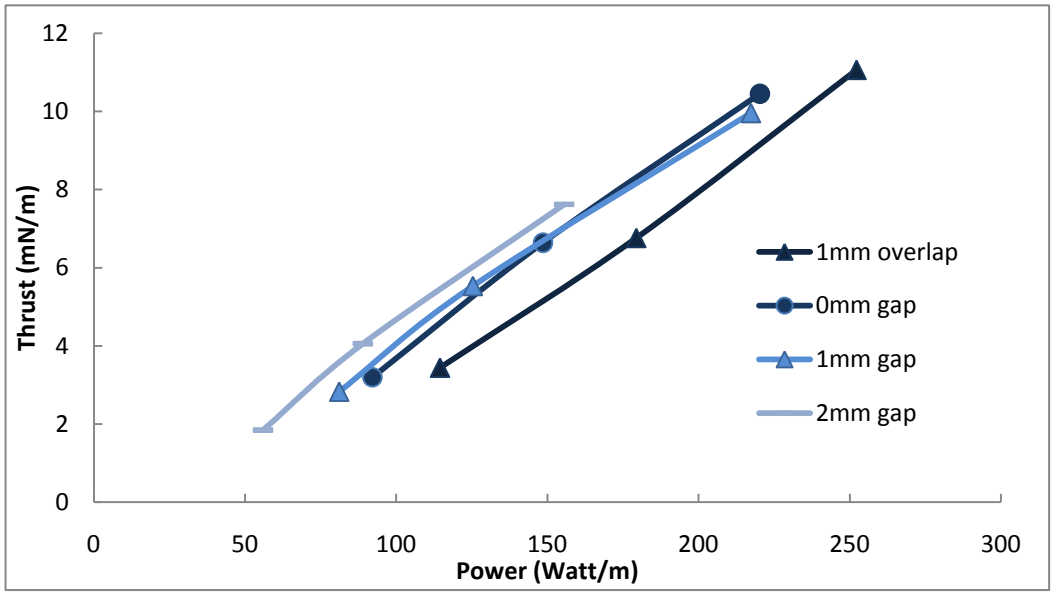

Figure 4.4: Thrust versus power input for various electrode gap sizes

4.1.3. Plasma actuator effectiveness for different exposed electrode geometries

To further study geometry effects comparisons were made between actuators constructed with tape and wire electrodes. The actuators used in this study were constructed using a 0.254 mm (0.01 inch) thick polyester film as the dielectric sheet, in a geometry similar to that of Hoskinson et al. [21].Figure 4.5 shows the various exposed electrode geometries that were tested, including two different thicknesses of wires, one with a 0.127 mm diameter and another with 0.1 mm diameter, as well as the typical tape electrode with a thickness of 0.089 mm. The gap between the electrodes remained at 1 mm in all cases, and the covered electrodes on the bottom were covered with Kapton tape.

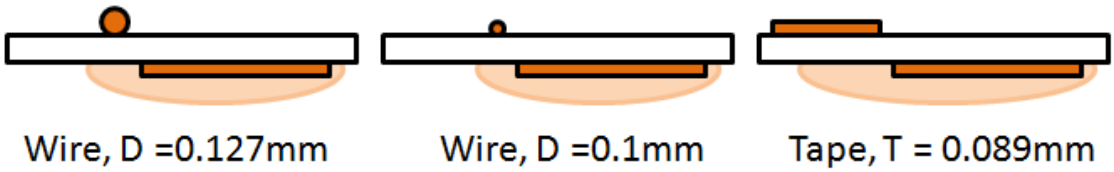

Figure 4.5: Schematic of plasma actuator setup for various exposed electrode geometries

The results of these measurements are shown in Figure 4.6.The applied voltage frequency was 1.0 kHz and the applied voltage magnitudes ranged from 10kV to 20kV, peak-to-peak. These measurements show that actuators constructed with a tape electrode of 0.089 mm thickness and a wire electrode of 0.127 mm diameter behave similarly. However, with a thinner 0.1 mm diameter wire, the actuator effectiveness is better than with the thicker 0.127 mm wire. This observation is consistent with the previous results from Hoskinson et al. [21] and Forte et al. [18]. As discussed by Forte et al., with a thinner exposed electrode, a stronger electric field is presented near the exposed electrode. Thus, the charge carriers are able to accelerate faster and more momentum is transferred to the neutrals particles. i.e. higher thrust is achieved.

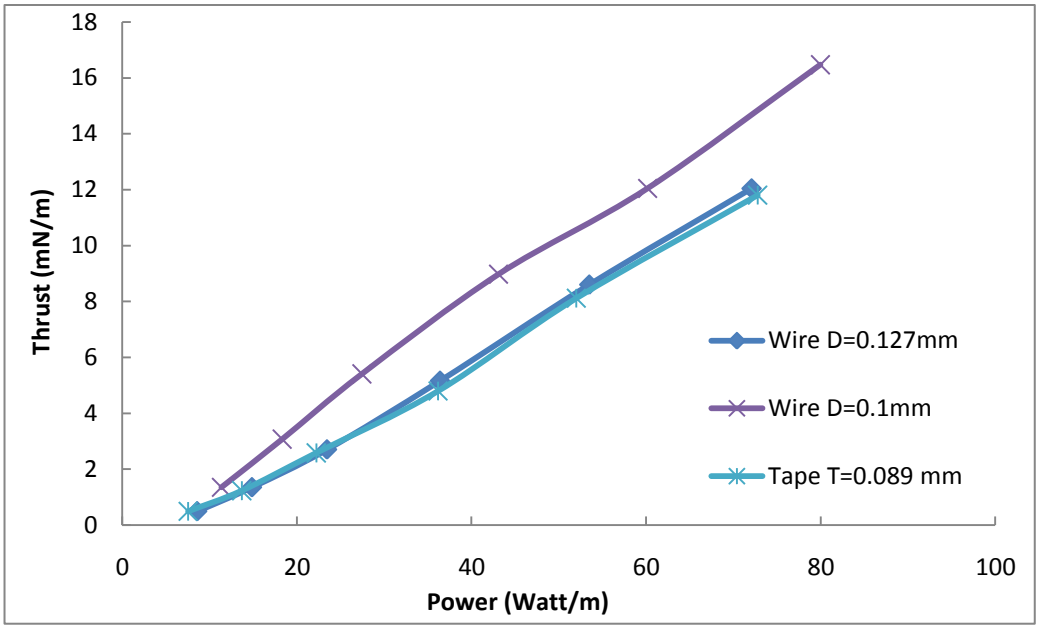

Figure 4.6: Comparison of actuators with different exposed electrode geometries

4.1.4. Plasma actuator effectiveness for different dielectric thicknesses

Experiments were also conducted to study the effects of dielectric thickness on actuator effectiveness. The actuators were constructed using copper tape electrodes with polyester dielectric film of various thicknesses, as shown in Figure 4.7. In order to get dielectrics thicker than 0.25mm, multiple layers of 0.254 mm thick polyester film were stacked together. While there may have been small air gaps between the polyester film layers, it was anticipated that the effects would be negligible as the plasma generated between the air gaps is much smaller and weaker than the plasma generated on the surface near the exposed electrode. Again, the gap between the electrodes remained at 1 mm for all cases, and the lower electrodes were covered with Kapton tape. The experiments were run at an applied voltage frequency of 1.0 kHz with applied voltage amplitude varying from 10kV to 20kV, peak-to-peak, (except for the 0.127 mm thick case, where the plasma actuator burned through the dielectric for applied voltages in excess of 16kV). The results of these studies are shown Figure 4.8.

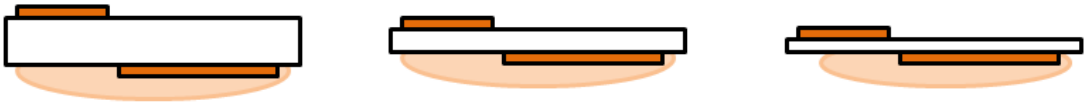

Polyester, T=1.02mm Polyester, T=0.25mm Polyester, T=0.13mm

Figure 4.7: Schematic of sample plasma actuator setup for various dielectric thicknesses

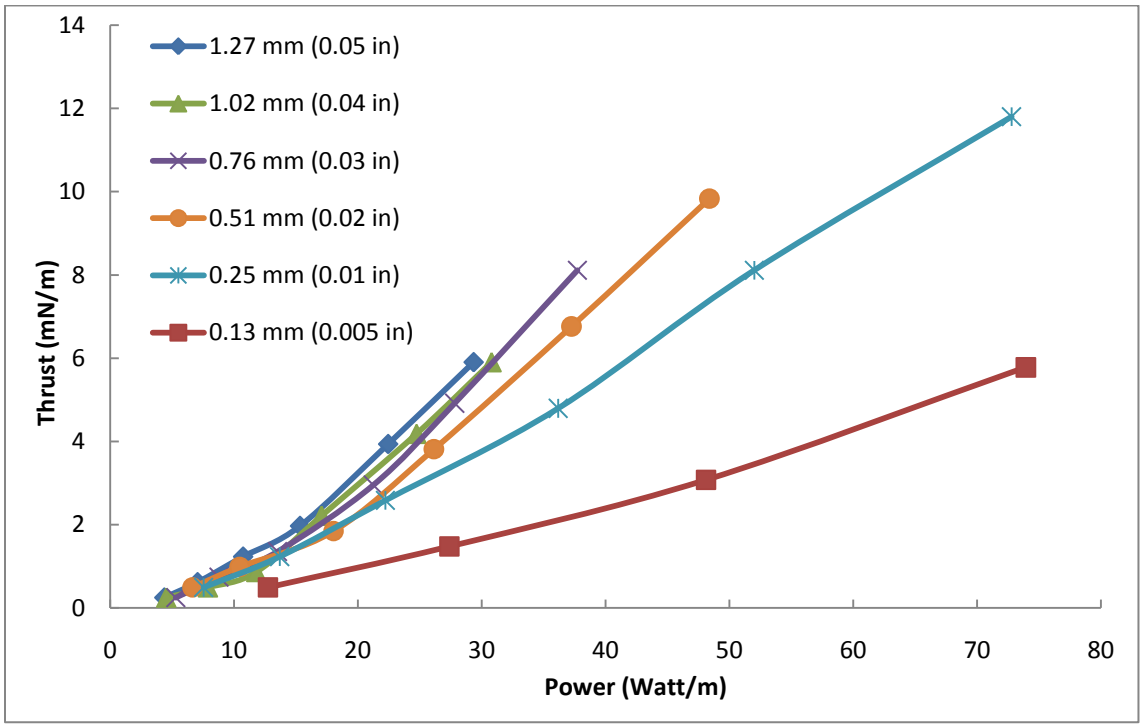

Figure 4.8: Comparison of dielectric thickness with plasma actuator performance

The results from Figure 4.8 can be used to determine the thrust as a function of dielectric thickness for a constant input power, as is done in Figure 4.9 for an input power of 29.5 Watt/m. This figure shows that plasma actuators with thicker dielectrics have higher effectiveness values.

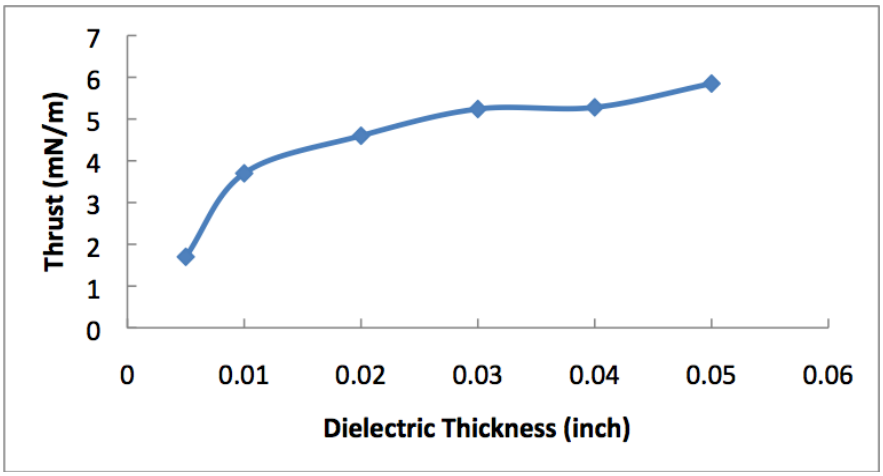

Figure 4.9: Thrust versus dielectric thickness at a constant input power of 29.5 Watt/m

However, when the measurements from Figure 4.8 are used to determine the thrust as a function of dielectric thickness for a constant applied voltage, as shown in Figure 4.10 for an applied voltage of 16kV peak-to-peak, the thrust generated by the plasma actuator is higher for a thinner dielectric. This is consistence with the Forte et al. results [18]. This suggests that the relation between thrust and dielectric thickness is not straightforward, requiring further analysis, as described in the next section.

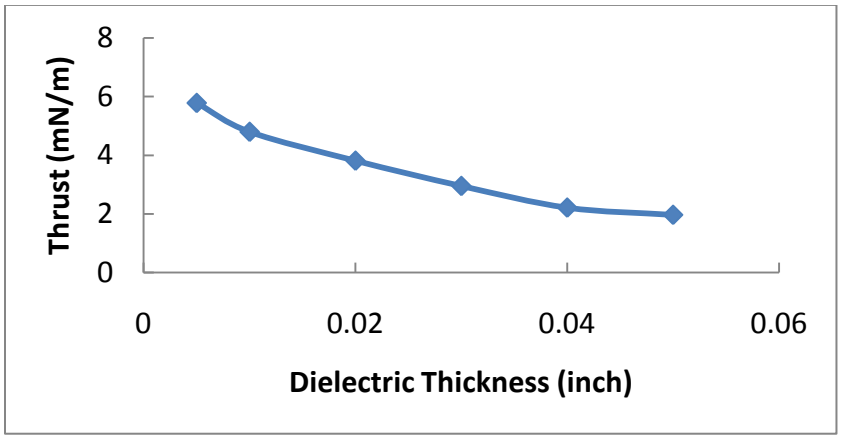

Figure 4.10: Thrust versus dielectric thickness at a constant applied voltage peak-to-peak amplitude of 16kV

4.2 Data Analysis

4.2.1 Thrust - plasma length data analysis

In order to better understand the previous results, it is useful to consider the effect of dielectric thickness on the asymmetry of the discharge between its two half cycles. Previous studies, including those by Enloe et al. [25], indicate a difference in the force generated by a plasma actuator between the two half cycles. Consequently, we conducted current-voltage characteristic and time-resolved ICCD optical measurements of the discharge during the positive current (backward) and negative current (forward) half cycles. We use the terms *forward* and *backward* to indicated positive ion directions. A comparison between the optical images of the two half cycles provides information about this discharge asymmetry. A typical result is shown in Figure 4.11 for a dielectric thickness of 1.27 mm (0.05 inch) and a power input of 25.57 Watt/m. Note that the image exposure time, indicated by the red trigger line, was 0.0005 sec (one half cycle) for each image, with the positive current half cycle monitored during the high level of the trigger line and the negative half cycle monitored during the low level of the trigger line.

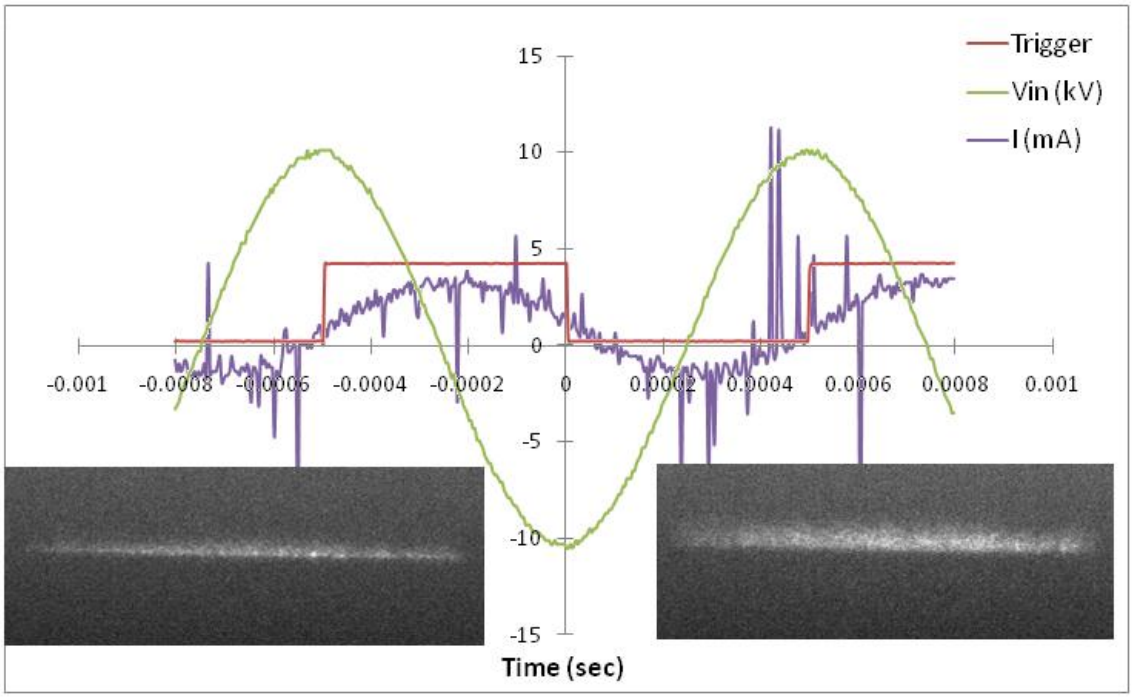

Figure 4.11: Comparison of optical measurements between current half cycles (left image taken in the positive current part of the cycle; right taken in the negative current part)

As Figure 4.11 shows, the plasma behaves asymmetrically between the two half cycles. This asymmetry may account, at least partially, for the resulting net thrust of the actuator. To explore this asymmetry in more detail, time-resolved optical measurements were taken to complement the performance measurements from Figure 4.9. For each case studied in Figure 4.9 the input power was at 29.5 Watt/m. Two images were taken representing the positive current cycle and the negative current cycle of the discharge. The results are shown in Figures 4.12 and 4.13. For Figure 4.12, each image was normalized to itself, thus allowing the details of the plasma structure in each image to be more apparent. This is evident from the stronger background signal present for images in which the maximum intensity is weaker. For Figure 4.13, all images were normalized together, allowing for comparison between images. In both figures, thrust increases for images higher up in the figure.

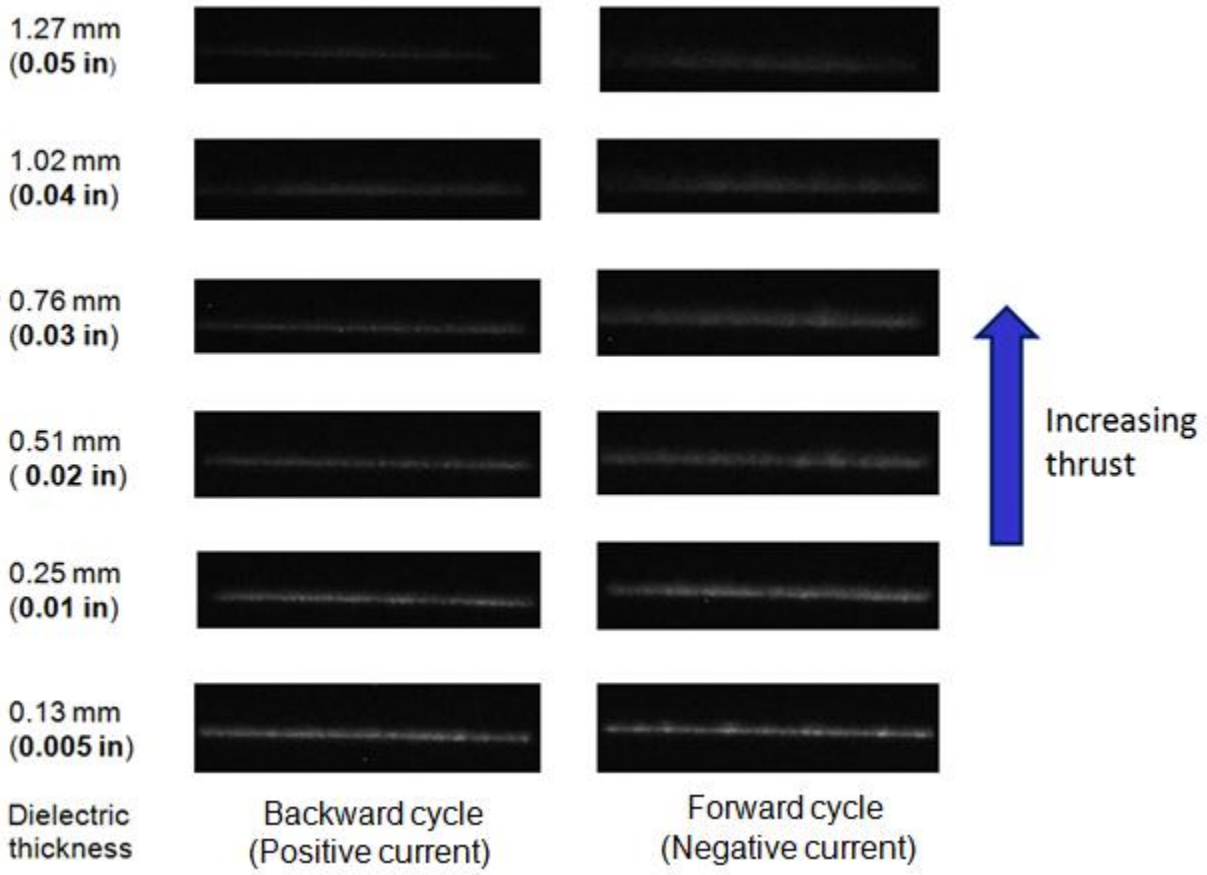

Figure 4.12: Optical image comparison between half cycles for different thicknesses with each picture's brightness normalized to itself.

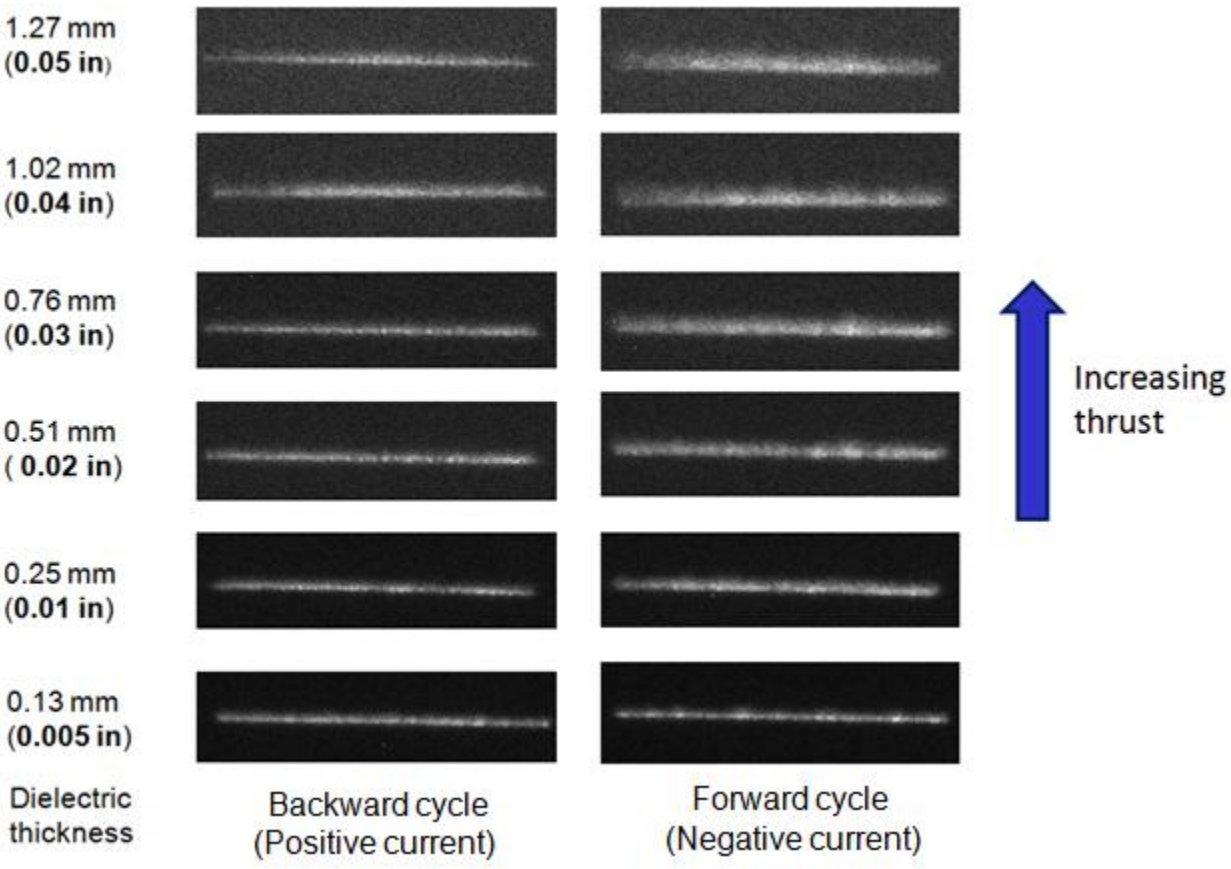

Figure 4.13: Optical image comparison between half cycles for different thicknesses when brightness is normalized in common between the pictures

From these figures, it is apparent that the plasma structure is significantly different between cases with thicker dielectrics and cases with thinner dielectrics. Although the plasma is dimmer with a thicker dielectric, as shown in Figure 4.12, the plasma extends further downstream during the negative current (forward) half cycle than during the positive current (backward) half cycle, as evident in both Figures 4.12 and 4.13. This enhanced length of plasma downstream for a thicker dielectric and resulting increased discharge asymmetry between the two half cycles could help account for the increasing thrust with increasing dielectric thickness observed under constant power input, as shown in Figure 4.9.

To confirm this hypothesis, a similar study was conducted at a higher constant power input of approximately 37kW/m. For this higher power, and hence a brighter discharge, the same trend was even more obvious, and easier to be studied. To further analyze the optical images and correlate these with the thrust measurements, we need to determine the average plasma length for each case. The average plasma length was determined from the intensity profiles of the ICCD images: several locations over the span of the plasma were selected from an ICCD image, then measured to get the average length of the plasma. An example of the intensity profile is shown in Figure 4.14.

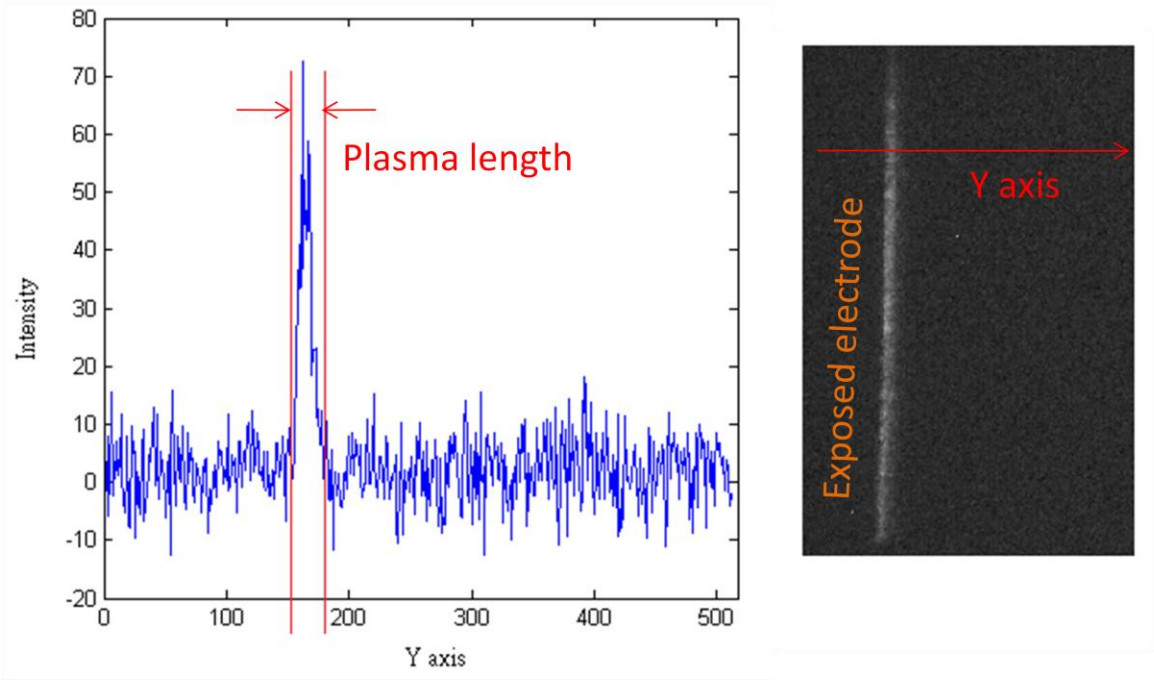

Figure 4.14: Example of intensity profile for ICCD image

The functional relationships between thrust and dielectric thickness and between the average plasma length during the negative current (forward) half cycle and the dielectric thickness were then studied. From Figure 4.15, it is clear that under constant input power conditions, an increase in dielectric thickness leads to both an increase in thrust and an increase in plasma length.

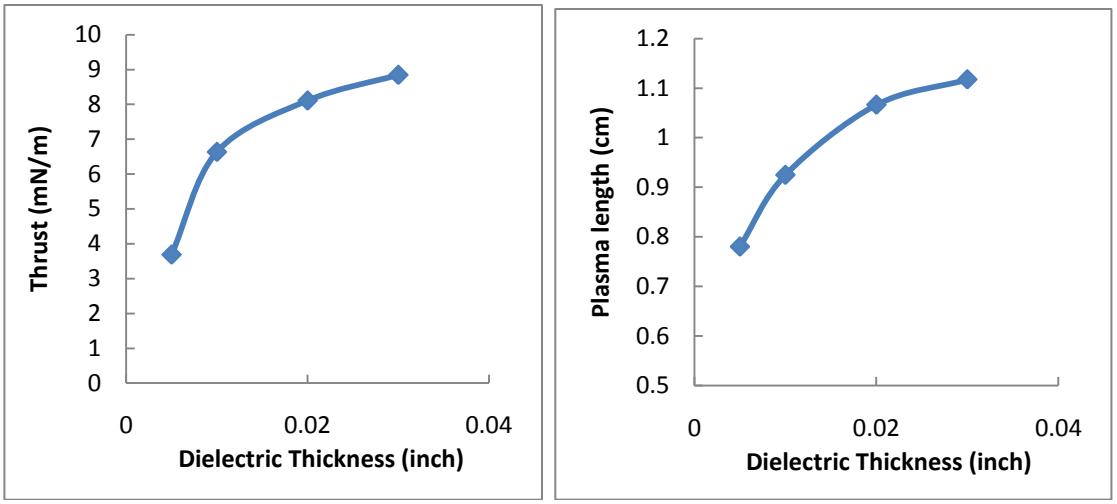

Figure 4.15: Thrust and plasma length versus dielectric thickness

By combining the plots in Figure 4.15, a clear correlation becomes evident between the thrust and the plasma length during the negative current (forward) half cycle, as shown in Figure 4.16. This figure suggests that the thrust and the plasma length are approximately linearly related. From the trend line of the plot, we can also extrapolate that when the plasma length during the negative current half cycle drops to about 0.5cm, the net thrust becomes zero. This length of the negative current half cycle plasma at zero net thrust compares favorably with the nearly constant positive current half cycle plasma length of 0.5-0.6 cm. These results demonstrate that the degree of asymmetry in the average plasma lengths between the two half cycles is related to the magnitude of the resulting net thrust, and hence the plasma actuator effectiveness.

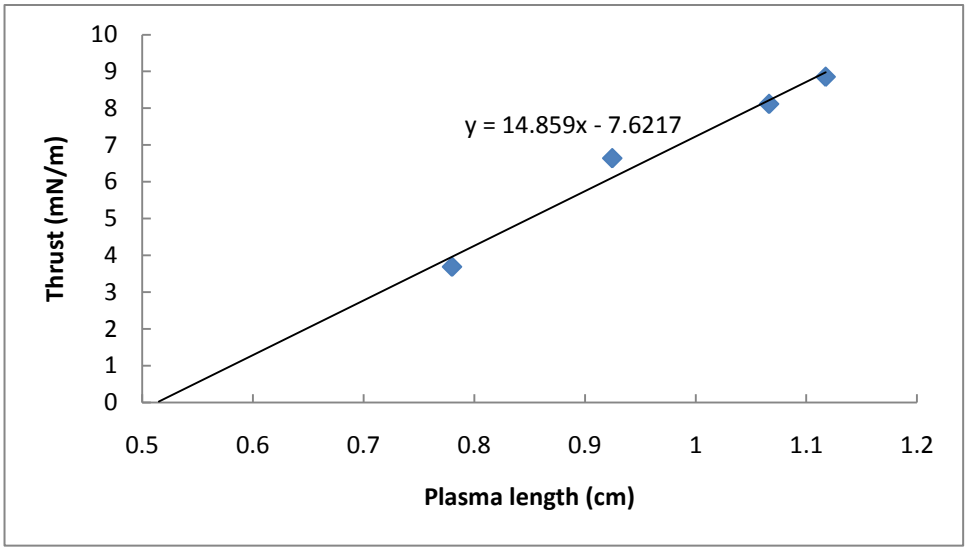

Figure 4.16: Thrust vs. plasma length during negative current (forward) half cycle

4.2.2 Relationships between applied power, plasma length and dielectric thickness

To explain the relation between the plasma actuator effectiveness and dielectric thickness, a simplified model was used to interpret the experiment. In this model, the plasma is assumed to be a good conductor, especially compared to the dielectric. A schematic of the plasma actuator and the simplified model is shown in Figure 4.17. As shown in the figure, the plasma overlapped with the covered electrode on the bottom. If the plasma is treated as a good conductor, then the dielectric would be acting like a capacitor with the length being the same as the plasma length. Thus, most of the power is stored in the dielectric.

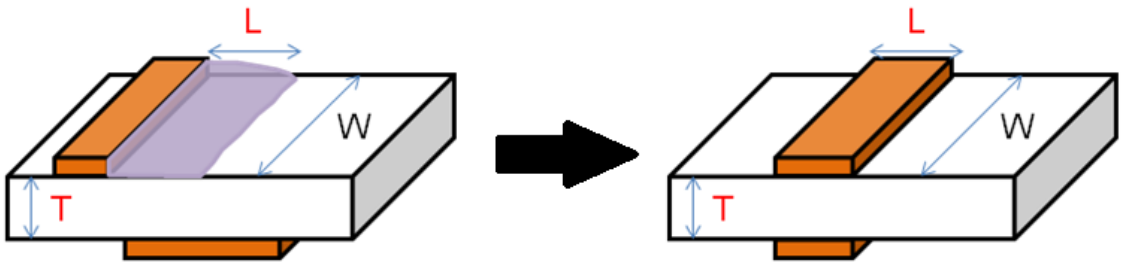

Figure 4.17: Plasma actuator schematic and simplified model

$(L = plasma\ lengt\square, W = plasma\ widt\square$ and $T = dielectric\ t\square ikness)$.

- **Comparison of plasma resistance and dielectric impedance**

First, in order to verify the validity of the assumption that the plasma is a good conductor compared to the dielectric and the appropriateness of this model, the plasma resistant was estimated and compared to the dielectric impedance. For this comparison, an equivalent circuit representation of the simplified model (Figure 4.17) was used, as shown in Figure 4.18. In this equivalent circuit model, the dielectric impedance includes a resistive component and a reactance component.

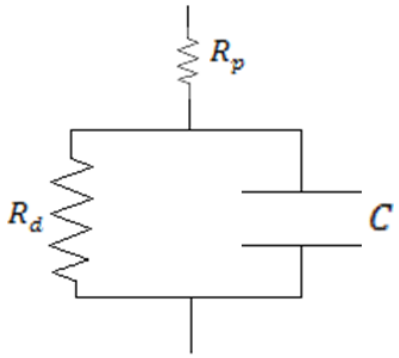

Figure 4.18. Equivalent circuit diagram for the simplified plasma actuator model (where R_d and C are the dielectric resistance and capacitance, and $R_p$is the plasma resistance)

To estimate the plasma resistance, R_p, we use the classical conductivity equation:

$$\sigma = \frac{n_e e^2}{m_e \nu_n} \tag{1}$$

where the electron density n_e is approximately 10^{15} cm^{-3} for a typical DBD [6], the elementary charge e is 1.6×10^{-19} C, and the electron mass m_e is 9.11×10^{-31} kg. The collision frequency, ν_n, is given by:

$$\nu_n = n_n \sigma_n \langle V \rangle \tag{2}$$

where the electron impact cross section, σ_n, in a weakly ionized plasma is typically of the order 10^{-20} m^2 [26]. At room temperature, the neutral density $n_n$is approximately 2.5×10^{19} cm^{-3}, and $\langle V \rangle$ is the mean velocity of the colliding

charged particle, in this case the electrons. The mean velocity, $\langle V \rangle$, can be found from the relation for the most probable speed, v_p, which can be determined from the electron temperature, T_e. For a typical microdischarge, T_e is in the range of 1eV [6].

$$\langle V \rangle = \frac{2}{\sqrt{\pi}} v_p = \frac{2}{\sqrt{\pi}} \sqrt{\frac{2kT_e}{m_e}} \tag{3}$$

These results yield a plasma conductivity, σ, of about 176 S/m. For the plasma geometry in our actuator, the plasma resistance is determined from the conductivity by:

$$R_p = \frac{L}{\sigma A} \tag{4}$$

For this analysis, it is further assumed that L is given by the plasma length and that the plasma cross sectional area is A_C= d x W, where d is the electrode thickness. Thus, for an electrode thickness, d, of 7.6×10^{-5} m and for an actuator width, W, of 0.09 m (typical for our actuator designs), the plasma cross sectional area, A_C, is approximately 7×10^{-6} m^2. Assuming a typical plasma length, L, based on our measurements of 0.01 m, then this results in an estimated plasma resistant, R_P, of approximately 4.1 Ω.

This value of R_P then needs to be compared to the dielectric impedance. Approximating the capacitance of the dielectric structure by a simple parallel plate capacitance model yields a capacitance of:

$$C = \varepsilon_r \varepsilon_0 \frac{A}{T} \tag{5}$$

Using a value of 4.1 for the relative permittivity, ε_r, of polyester, the vacuum permittivity, ε_0, = 8.854×10^{-12} F/m, a plasma surface area of A_S = L x W = 9×10^{-4}

m^2 and a dielectric thickness, T, of 0.3 mm, the capacitance of the dielectric structure is approximately 6.64×10^{-11} F.

The reactance component of the dielectric impedance can then be found from:

$$X = \frac{1}{\omega C} \tag{6}$$

where the angular frequency is $\omega = 2\pi f$. Thus, using the typical value of 1 kHz for the frequency, f, (for our experiments), the reactance is approximately 2.4×10^6 Ω. Finally, for the resistance part, $R_{d,}$ of the dielectric impedance: a typical insulation resistance of a dielectric capacitor is in the range of gigaohm [27]. Thus, for our sample calculation, 10^9Ω is used for $R_{d.}$

As shown in Figure 4.18, the equivalent impedance of the dielectric structure is found by combining these two parallel components, X and R_d, yielding a dielectric structure impedance of approximately 5.7×10^3 + j -2.4×10^6 Ω. From this, it is clear that the dielectric behaves primarily as a capacitor.

Comparing the dielectric structure impedance of 5.7×10^3 + j -2.4×10^6 Ω to the plasma resistance of 4.1 Ω, also indicates that the plasma is indeed quite conductive compared to the dielectric. This confirms our modeling assumption that the plasma is a good conductor compared to the dielectric and the appropriateness of this model for our future analyses.

- **Resulting Relationships**

From this model, we see that part of the dielectric behaves like a capacitor. In order to determine the relation between the plasma actuator effectiveness and the dielectric thickness, the complex power, S, is considered:

$$S = P + jQ \tag{7}$$

where the actual power, P, is the input power we measured in the experiments, and reactive power, Q, is due to the capacitive characteristic of the dielectric structure.

The complex power equation is given by:

$$S = \frac{{V_m}^2}{2}\frac{1}{Z^*} \tag{8}$$

where V_m is the applied voltage magnitude, Z is the combined circuit impedance, and Z^* is the complex conjugate of the combined circuit impedance.

The combined circuit impedance, Z, for the equivalent circuit shown in Figure 4.18 is

$$Z = R_p + Z_d \tag{9}$$

Where the impedance of the dielectric structure, $Z_{d,}$ is given by

$$Z_d = R_d \parallel \frac{1}{j\omega C} \tag{10}$$

Using Equation 10 in Equation 9 yields

$$Z = \left[R_p + \frac{R_d}{1+(R_d\omega C)^2}\right] + j\left[\frac{-{R_d}^2\omega C}{1+(R_d\omega C)^2}\right] \tag{11}$$

Substituting this result for Z in Equation 8, yields for the complex power

$$S = \frac{{V_m}^2}{2}\left[\frac{R_p+x}{\left(R_p+x\right)^2+(xR_d\omega C)^2}\right] + j\frac{{V_m}^2}{2}\left[\frac{-xR_d\omega C}{\left(R_p+x\right)^2+(xR_d\omega C)^2}\right] \tag{12}$$

where x is defined as:

$$x = \frac{R_d}{1+(R_d \omega C)^2} \tag{13}$$

Then, the actual power is obtained from the real part of the complex power,

$$P = \frac{{V_m}^2}{2}\left[\frac{R_p+x}{\left(R_p+x\right)^2+(xR_d\omega C)^2}\right] \tag{14}$$

and the reactive power is obtained from the imaginary part of the complex power,

$$Q = \frac{{V_m}^2}{2}\left[\frac{-xR_d\omega C}{\left(R_p+x\right)^2+(xR_d\omega C)^2}\right] \tag{15}$$

For the previously determined values for C, Rp, and Rd, as well as for Vm = 10 kV and a frequency of 1 kHz, the actual power, P, determined from Equation 14 is approximately 0.05 Watt and the reactive power, Q, determined from Equation 15 is approximately -20.8 var (volt-amperes reactive). Since the calculated actual power is two orders of magnitude smaller than our experimental results (5 Watt), this would suggest that the actual dielectric is slightly lossy. However, the reactive power is clearly much larger than the actual power. Once again, this confirms our model assumptions that the plasma actuator behaves primarily like a capacitor, storing most of the energy transferred to it instead of dissipating the energy within the plasma discharge.

To derive an approximate relationship between the plasma length, dielectric thickness and applied voltage, the actual power (Equation 14) is rearranged such that the actual power is proportional to the square of the applied voltage and to the plasma length, L, and inversely proportional to the dielectric thickness, T, as:

$$P \propto \frac{{V_m}^2 L}{T} \tag{16}$$

Thus, under constant power:

$$V^2 L \propto T \tag{17}$$

Now a V^2L versus T plot of the constant power experiment results at 37 W/m (diamonds) and a best linear fit to these results (solid line) are shown in Figure 4.19. This figure demonstrates that the experimental results are consistent with the functional relationship derived from the model in Equation 17.

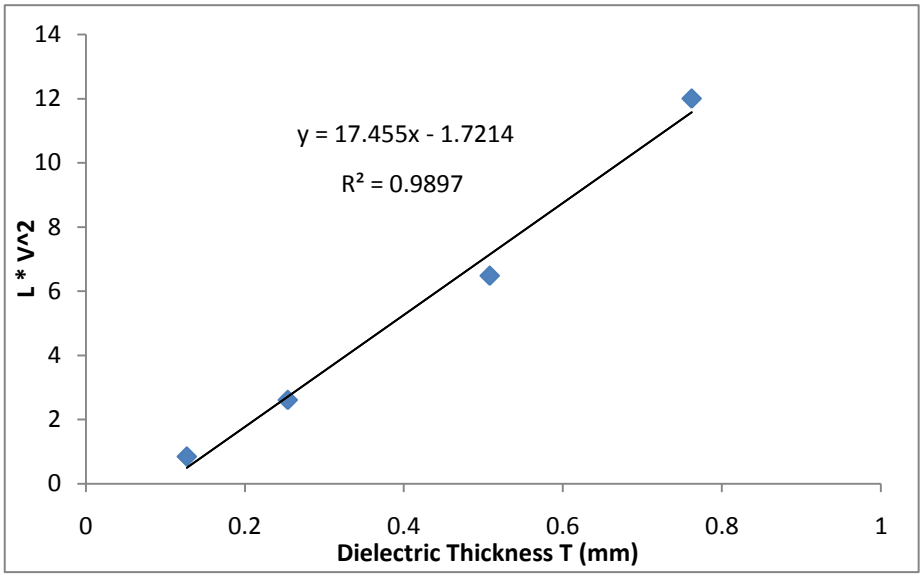

Figure 4.19: Relationship between dielectric thicknesse, plasma length and applied voltage

Determination of the correct applied voltages needed to maintain a fixed power as the dielectric thickness is varied could be simplified if a relationship can be established between the applied voltage and the dielectric thickness under constant power. Without this relationship, determination of the needed voltages requires that a series of experiments be performed. First, the performance curve

of the plasma actuator, the plot of thrust versus dielectric thickness for various applied voltages (such as Figure 4.8), must be measured and then from these results the set of applied voltages needed to maintain a fixed power as dielectric thickness is varied must be extrapolated.

To determine such a relationship, first consider the relation between the dielectric thickness and plasma length determined in our experiments, as shown by the diamonds in Figure 4.20.

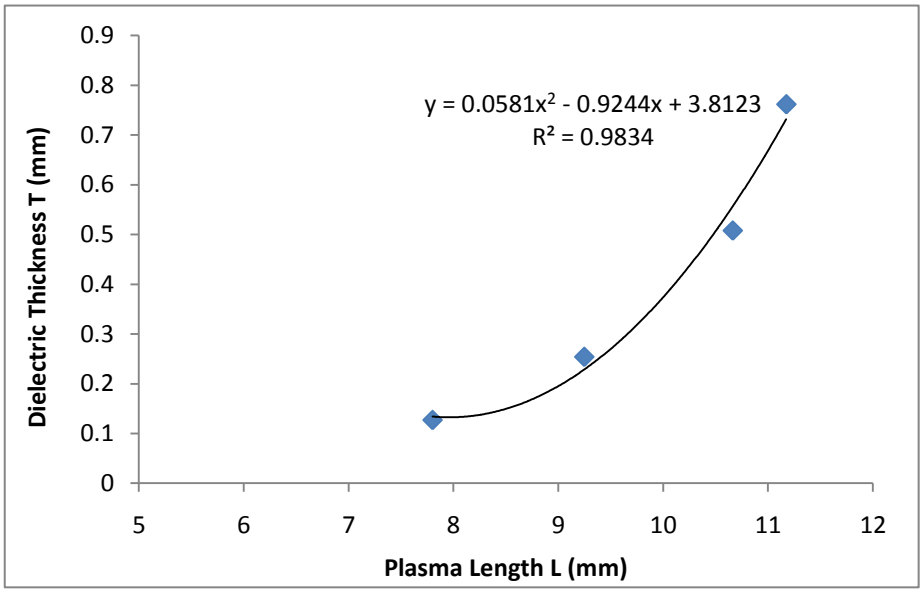

Figure 4.20: Relation between plasma length and dielectric thickness

As shown by the solid curve in Figure 4.20, these data are well represented by a quadratic relationship between the dielectric thickness and plasma length, i.e.:

$$T \propto L^2 \text{ or } L \propto \sqrt{T} \tag{18}$$

Now, combining relations (17) and (18) yields for the relation between the applied voltage and the dielectric thickness:

$$V^4 \propto T \text{ or } V \propto T^{\frac{1}{4}} \tag{19}$$

The experimental results (diamonds) shown in Figure 4.21 indeed confirm this relationship as indicated by the quadratic best fit to the data (solid curve)

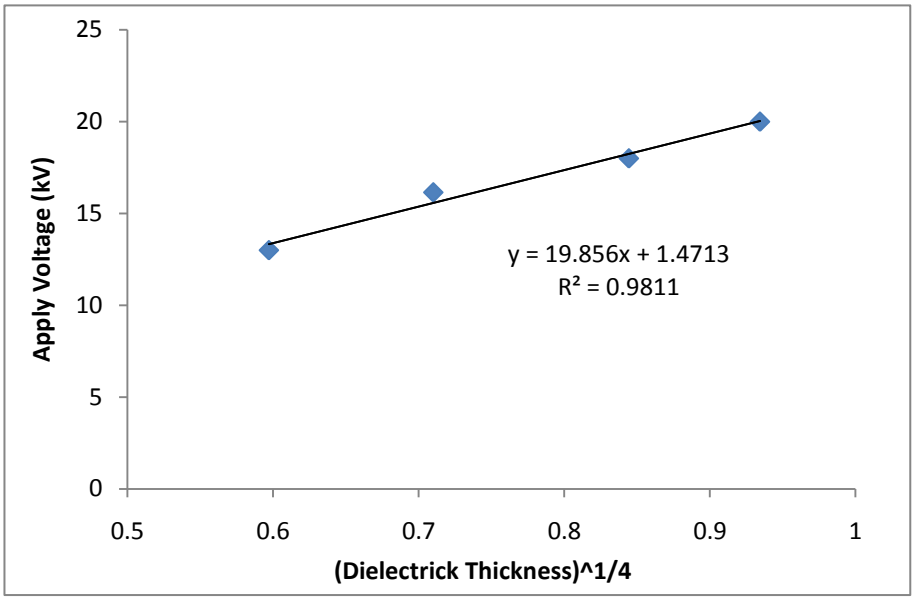

Figure 4.21: Relation between apply voltage and dielectric thickness

Then, from this relationship, the applied voltage for various dielectric thicknesses at a constant power can be easily calculated.

- **Alternative Analysis**

As mentioned previously, the power measured from experiment is two orders of magnitude larger than the actual power calculated from the previous model analysis However, it is suspected that the actual plasma resistant is much higher than the plasma resistant estimated in the previous analysis, as a consequence of the narrow structure of the microdischarges. For example, taking an Rp of 500000 Ω yields a calculated actual power P (Equation 14) of approximately 4 Watt, which is much more comparable to the experimental results.

Using this larger value for Rp, the actual power term can be derived in a manner similar to that shown in the previous section, yielding for the relation between the actual power, applied voltage amplitude and plasma length as:

$$P \propto \frac{V^2}{L} \tag{20}$$

Again, under constant power:

$$V^2 \propto L \tag{21}$$

Now a V^2 versus L plot of fhe constant power experiment results at 37 W/m results (diamonds) and a best linear fit to these results (solid line) are shown in Figure 4.19. This figure demonstrates that the experimental results are consistent with the functional relationship derived from the model in Equation 21.

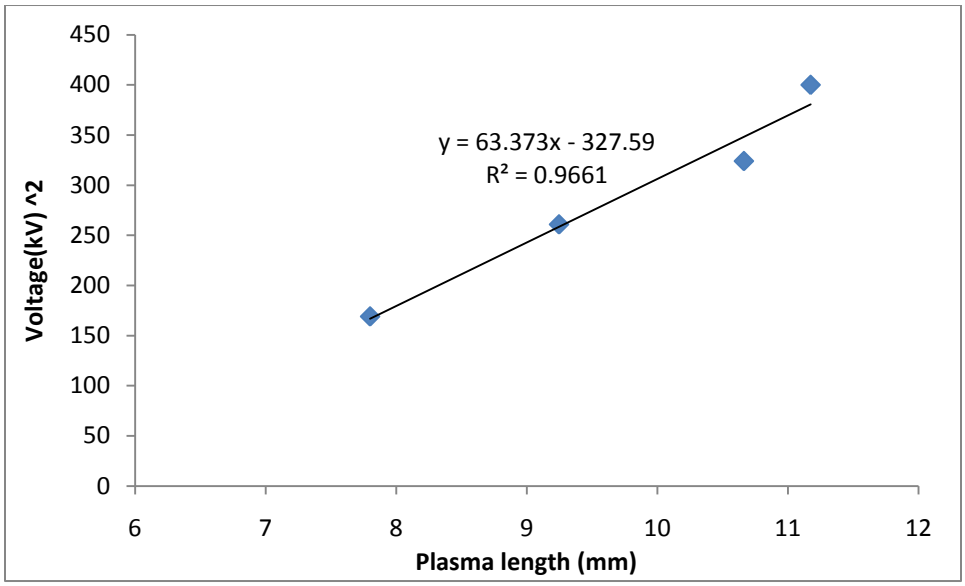

Figure 4.22: Relationship between applied voltage and plasma length

Then, combining Equation 21 with the empirical relationship given by Equation 18, yields for the relation between the applied voltage and dielectric thickness:

$$V^4 \propto T \text{ or } V \propto T^{\frac{1}{4}} \tag{22}$$

This turns out to be the same as the relationship derived from the previous analysis (Equation 19).

Now comparing the relations determined from the first analysis, Equations 16 and 17, with the relations determined from the second analysis, Equations 20 and 21, it is seen that the dielectric thickness is no longer a factor in these relationships under the assumption in the second analysis of a much larger value of Rp. From Equation 21, the second analysis indicated that the relationship between the applied voltage and the plasma length $\frac{V^2}{L}$ should be independent of the dielectric thicknesses. However, as shown in Figure 4.23, the experimental results indicate otherwise, suggesting this model does not fully represent the physical situation.

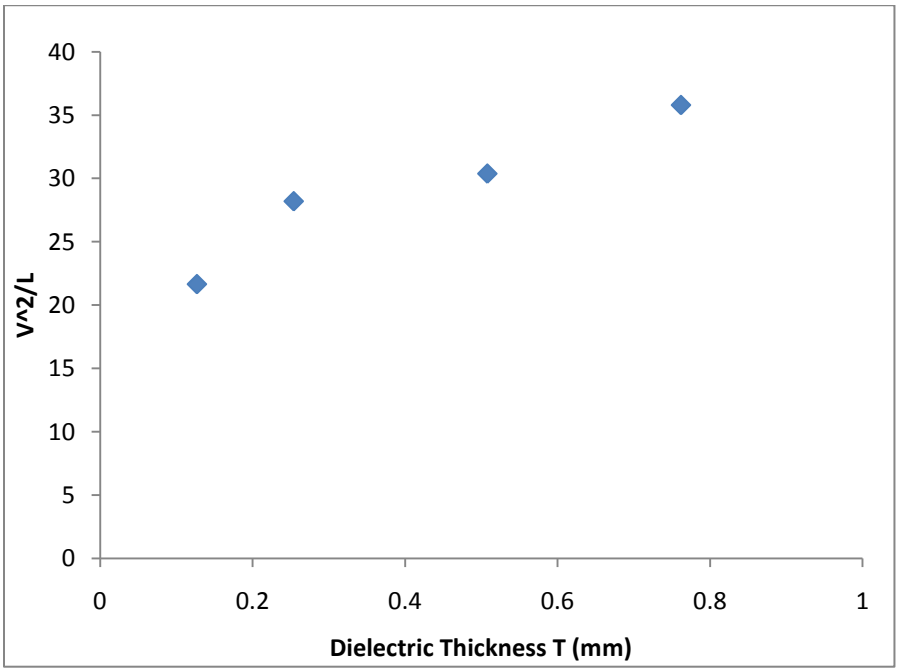

Figure 4.23: Relationship between applied voltage, plasma length and dielectric thickness

- **Discussion**

The first analysis treated the plasma as a uniform good conductor along the width W of the electrode, yielding a plasma actuator performance that is primarily based on the dielectric impedance. However, this analysis ignored the fact that the DBD discharge actually consists of many micro-discharges. A typical micro-discharge channel has a radius of 50-100μm [6], resulting in a plasma resistance

that is much higher than for the uniform plasma case. This is the reason that the actual power derived in the first analysis was two orders of magnitude lower than the experimentally measured power.

Similarly, while the second analysis, using a much higher plasma resistance, results in a calculated actual power term much closer to the experimentally measured value, it ignores how the plasma resistant is also affected by other factors. Such complicating factors include the plasma length variation with dielectric thickness and the detailed time variation of the plasma length., Lack of consideration of such factors thus results in an inconsistency between the results of this second analysis and experimental results.

However, despites drawbacks in each these two analyses, they both eventually lead to the similar conclusions. This suggests that a more accurate model for the plasma actuator would actually be a combination of these two approaches, where the plasma resistant is more accurately represented.

4.3 Summary

The performance of plasma actuators were studied for actuators constructed utilizing different electrode geometries and dielectric thicknesses. The effect of the dielectric thickness on plasma actuator effectiveness was explored in some detail. A simplified model was developed which indicated that the bulk of the energy transferred to the actuator is stored in the dielectric structure instead of being consumed in the plasma discharge. Furthermore, for constant power experiments and assuming a uniform plasma, the relationship between the dielectric thickness, plasma length and applied voltage amplitude is found to be $V^2 L \propto T$. However, it was also determined that for a more accurate model one needs to consider that the DBD plasma structure actually consists of many of micro-discharges, resulting in a much higher plasma resistance.

Chapter 5. Future Work

From these and earlier studies including those by Enloe et al. [25], it is clear that the plasma structure is a factor which affects generated thrust. The plasma structure, such as the uniformity of the plasma, can be manipulated by changing the plasma actuator geometry as demonstrated by this research. The commercial copper tape that was used for the electrodes in this study had sharp edges that caused non-uniformities along the span-wise direction in the plasma discharge. Further improvements on actuator effectiveness could be realized by implementing the following design modifications.

5.1 Exposed electrode with dielectric shielding design

One approach to reducing the effect of any electrode non-uniformity might be to add dielectric shielding to the exposed electrode, as shown in Figure 5.1. It is anticipated that with a thin dielectric coating covering the rough electrode, a more uniform plasma will form on the smoother shielding surface than occurs on the non-uniform edge of a copper tape electrode. The dielectric coating must be thinner then the dielectric coating on the covered electrode so that the plasma forms on the desired side. We tried an epoxy adhesive for the dielectric coating as an initial test of this technique, but the material could not withstand the plasma temperature and melted shortly after the plasma ignited. Air bubbles under the dielectric shielding were the suspected cause, leading to the melting of the epoxy shielding. High temperature electrically-resistant ceramic adhesives (Cotronics Resbond 919 and Cotronics Resbond 920) were also tested as a potential dielectric shielding material; however, this material also burned under normal operating conditions. Both of these ceramic adhesives can withstand a temperature of 1500 degrees Celsius. Since the DBD is a non-thermal plasma where the gas temperature is not nearly this high, the burn-through of the dielectric shielding is likely not due to high temperature. It is suspected that the

burn-through could be caused by plasma etching of, and damaging to, the dielectric shielding. Thus, in order for this idea to work, a more suitable material must be found and tested for dielectric shielding.

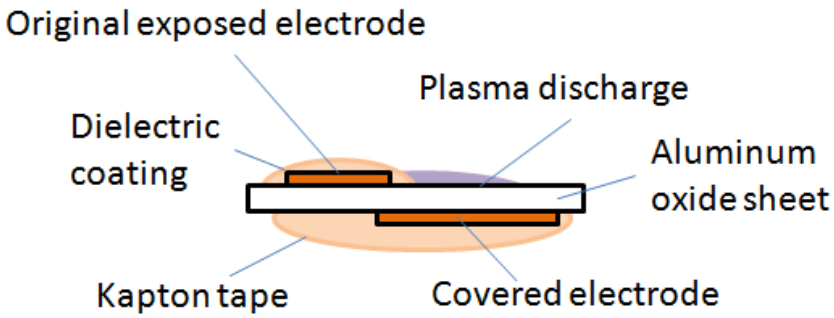

Figure 5.1: Exposed electrode with dielectric coating

5.2 Deposited exposed electrode design

Another approach to reducing the relatively rough surface and edge present for a copper tape electrode that results in non-uniformities in the plasma discharge might be to use thin film metal deposition for forming the exposed electrode. For initial testing, we constructed plasma actuators using an electroplating technique to generate a copper film as the exposed electrode. With this technique, the electrode surface and edges should be much more uniform compared to those of the copper tape. To do this, 200 Å of Ti was first sputtered onto the aluminum oxide dielectric sheet as an adhesive layer followed by the sputtering of 2000 Å of Cu onto the Ti for a seed layer. The Cu film was then grown to a thickness of 1 µm using an electroplating technique. The reason or combining the sputtering technique with the electroplating technique was because it was a relatively inexpensive and easy way to deposit a 1 µm Cu film. For example, directly sputtering a 1 µm film can often cause the film to crack.

ICCD images from plasma actuators built with exposed electrodes formed by this technique were taken by the experimental setup shown in Figure 5.2 to determine if there were any differences between the characteristics of these actuators and those constructed using copper tape exposed electrodes. In this

set of experiment, both electrodes were not covered with dielectric tape. Thus, there were discharges on both side of the plasma actuator, as shown in Figure 5.2 This is for the purpose of comparison between the copper tape exposed electrode and deposited exposed electrode.

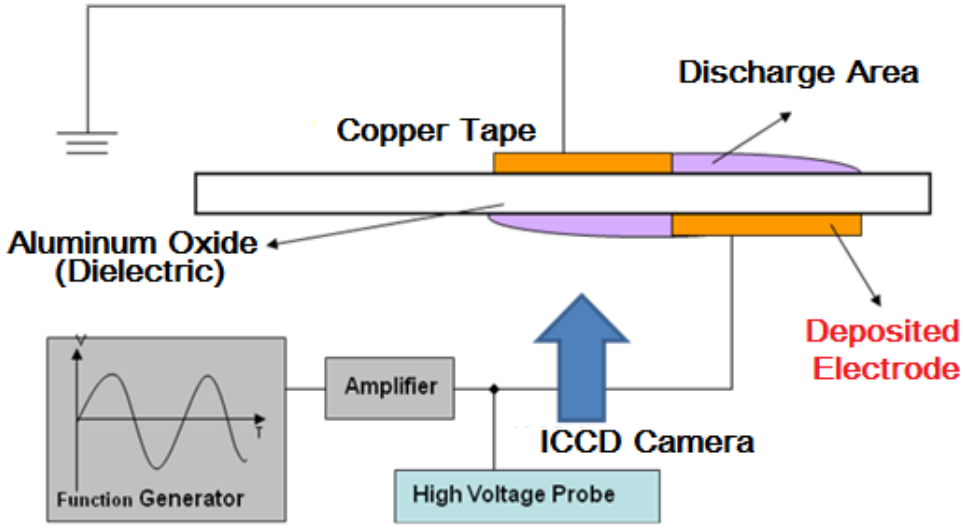

Figure 5.2: Plasma actuator setup

(Note that the ICCD images were taken on the deposited electrode side.)

Figure 5.3 shows a typical current-voltage characteristic plot and ICCD image of the deposited exposed electrode plasma actuator. Note that because of the symmetry of the plasma actuator used in this measurement, as shown in figure 5.3, the current is symmetric as well.

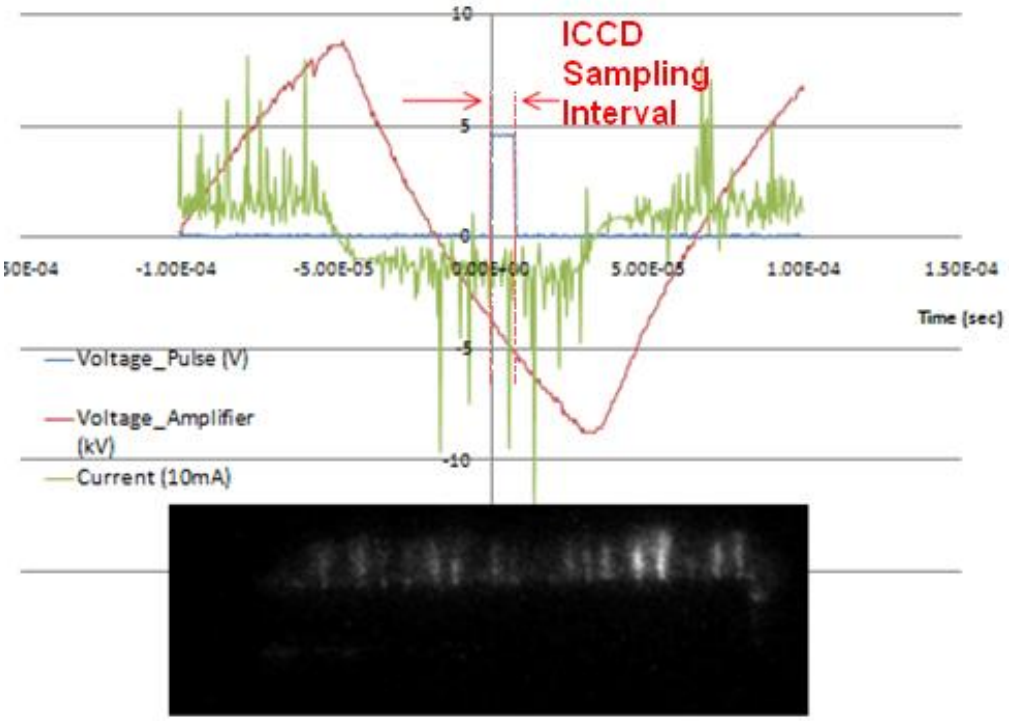

Figure 5.3 :Characteristics of a deposited film plasma actuator

$V_{in(p-p)}$ = 17.2 kV; frequency = 6 kHz; air at 760 Torr

Previous results for a copper tape exposed electrode design (Chapter 3.) showed that the plasma is normally more filamentary during the positive current half cycle (when electrons are traveling from the exposed electrode to the dielectric). Figure 5.4a compares the plasma generated with the copper tape exposed electrode design and the deposited exposed electrode design during this half cycle. A more "uniform" filamentary plasma is observed with the deposited electrode, as shown in Figure 5.4a. During the negative current half cycle (when electrons are moving from the dielectric to the exposed electrode) the plasma is normally more uniform, and Figure 5.4b demonstrates that there is little difference between these two designs during the negative current half cycle.

These results show that there is an overall improvement in the uniformity of the plasma for a plasma actuator constructed using deposited film electrodes. It is anticipated that the thrust generated by such an actuator should be more uniform

as well. However, the plasma actuator we constructed using the deposited exposed electrode design malfunctioned before thrust measurements could be completed. Thus, we could not do a comprehensive effectiveness experiment for this design. Upon inspection, the malfunction resulted from the deposited electrode peeling off from the dielectric substrate, indicating that this combined sputtering and electroplating method does not provide a mechanically stable electrode. However, another post processing technique, such as thermal annealing the deposited electrode, might make the deposited electrode more stable and should be investigated.

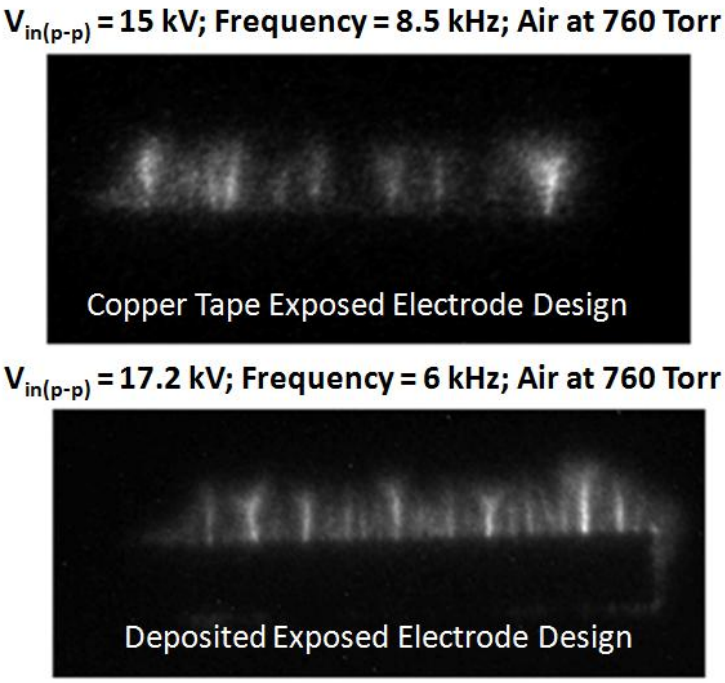

Figure 5.4a- Comparison of plasma emission during the filamentary positive current half cycle

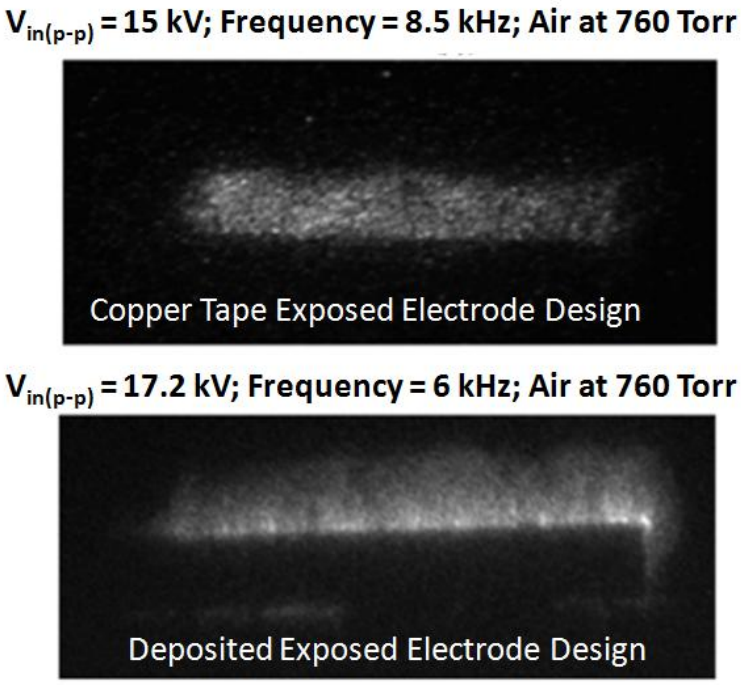

Figure 5.4b: Comparison of plasma emission during the uniform negative current half cycle

5.3 Micro-scale exposed electrode design

Once a more stable method for forming a deposited electrode is found, further modification of the exposed electrode could be tested. According to Thomas et al. at the University of Notre Dame, using a macro-scale (3 mm) triangular shaped exposed electrode edge for the actuator's exposed electrode yields higher thrust [28]. This is likely due to the triangle-shaped points generating a locally concentrated electric field. The thrust is generated by the collisions between the charge carriers and the neutrals particles. An enhanced electric field could lead to a higher thrust from the plasma actuator; thus, it could increase the plasma actuator effectiveness. Hershkowitz et al. at the University of Wisconsin tested micro-scale wire electrodes (diameter of 25 microns) and found that they yield uniform discharges with higher thrust. It is hypothesized that this is possibly due to field emission caused by the enhanced electric field near the small diameter wires. Thus, by combining a micro-scale triangular-shaped exposed

electrode edge with a thin electrode, it might be possible to generate high electric fields (near or at field emission strength) achieving higher thrust. In addition, by having micro-scale triangles at the edge, the micro-discharge density should be increased, further enhancing effectiveness. Since a typical micro-discharge channel has a radius of 50-100μm [6], it was theorized that, to optimize the thrust per area, the distance between the triangular edge points (dimension A in Figure 5.5) should be around 200 μm. Thomas et al. find out that for the macro-scale triangular shaped exposed electrode has a optimum performance when the ratio of B/A=4. Applying this to the micro-scale triangular shaped exposed electrode suggests that the length of the individual triangle (dimension B in Figure 5.5) should be around 800 μm. The electrode thickness, T, should be around 25 μm.

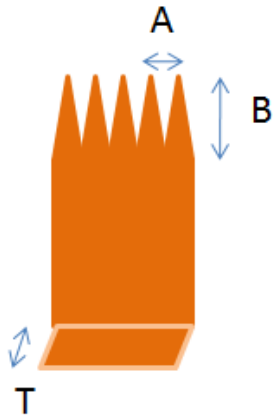

Figure 5.5: Micro-scale, triangular-shaped, exposed electrode edge geometry

Since considerable time and cost is needed to fabricate an actual triangular-edged electrode, for preliminary testing the micro-scale exposed electrode design was approximate by constructing the exposed electrode from fine copper wire screen meshes. With screen meshes, we were able to easily focus on investigating the spanwise structure of the discharge while varying the spacing between the edge points (dimension 'a' in Figure 5.5) by changing the size of the wire mesh.

The objective of the first set of experiments was to optimize the actuator effectiveness with respect to various wire mesh sizes. We used a series of wire meshes with mesh sizes of 40, 60, 80, and 100, where the number represents the number of openings per inch, as shown in Figure 5.6. Wire meshes of sizes 40, 60, 80, and 100 have openings (spacing between wires) of 635 µm, 423 µm, 318 µm, and 254 µm, respectively.

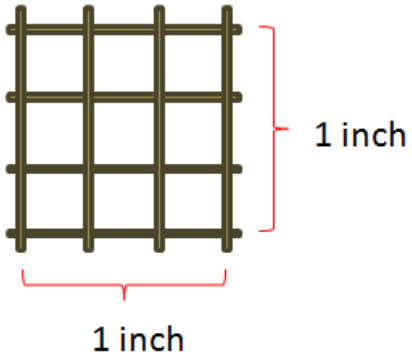

Figure 5.6: Example of size 3 wire mesh (3 opening per inch)

The results of thrust measurements for plasma actuators constructed using these wire-mesh exposed electrodes are shown in Figure 5.7, where they are also compared with data for the original tape exposed electrode design. These measurements were conducted using a standard actuator configuration with a 0.5 mm (0.02 inch) thick PMMA dielectric, such as the ones in Figure D-7. The covered electrode was covered with Kapton tape to prevent a discharge on that side of the actuator. There was a 1 mm overlap between the trailing edge of the exposed electrode and the leading edge of the covered electrode. The frequency of the applied voltage for this set of experiment was 1.0 kHz, with the applied voltage varying from 10 kV to 20 kV peak-to-peak.

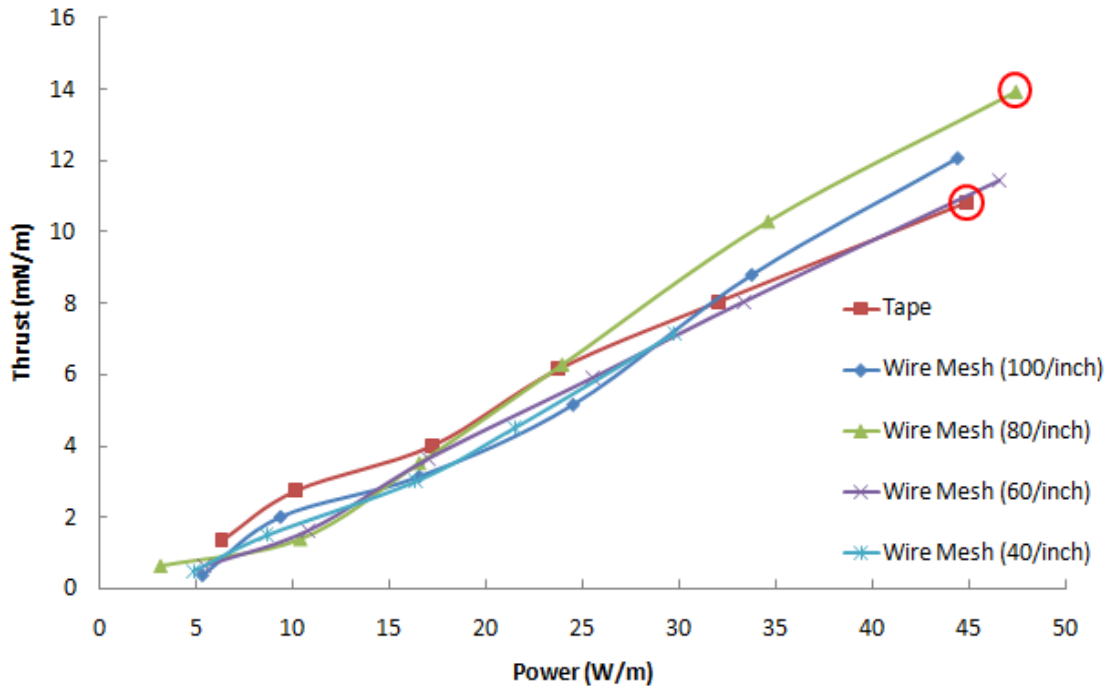

Figure 5.7: Thrust vs. power input for mesh electrodes of varying sizes and for a tape electrode

These results show that the highest thrust is achieved with a wire mesh of 80 spaces per inch (318 µm openings). From theory, the optimal spacing between edge points (dimension 'a' in Figure 5.5), which also corresponds to the distance between each wire, was calculated to be around 200 µm. This would suggest that 100-mesh screen should give the highest thrust. Although the results shown in Figure 5.7 indicate that a slightly larger opening (spacing between wires) of 318 µm yields the highest thrust, this is reasonably close to the optimal spacing computed by the simple theory.

For an applied voltage of 20kV peak-to-peak, the thrust increased from 10.8 mN/m for the tape electrode design to 14 mN/m for wire mesh electrode design with a mesh size of 80, as indicated by the red circles in Figure 5.7. This demonstrates an approximately 30% improvement in thrust when going from a tape electrode to an 80-mesh (318 µm spacing) wire screen electrode. These

results also show that as the mesh sizes decrease below 80 spaces per inch, the effectiveness decreases. But in addition, when the wire meshes per inch increase above 80, the effectiveness also decreases and eventually becomes similar that of a tape exposed electrode. A possible explanation for these observations is that for an opening larger than about 300 μm, the plasma is not as concentrated over the spanwise direction, leading to decreased effectiveness. While, when the wire mesh opening is too small, such as for a size 100 spaces per inch mesh (254 μm spacing), the distance between each wire becomes close enough that neighboring micro-discharges interact, reducing the effectiveness.

- **Combined micro-scale electrode design with other designs**

While the 30% improvement in thrust achieved utilizing a micro-scale exposed electrode versus a tape electrode is not of major significance by itself, in combination with other design improvements (e.g., third-electrode, diodes, silicon thin film) investigated by our research group [29] it is anticipated that this can help to significantly improve the overall effectiveness of plasma actuators.

To confirm this hypothesis, studies are currently underway to test the micro-scale wire mesh electrode approach on a three-electrode plasma actuator design (which uses an amorphous silicon (a-silicon) layer and diodes, as shown in Figure 5.8), by replacing the exposed tape electrode on the left side by a wire mesh electrode. The three-electrode plasma actuator is a novel design which has been demonstrated to manipulate the surface charge on the dielectric to enhance the generated thrust, resulting in an increase in thrust of up to 70%. By combining this design with the mesh electrode, it is expected that the effectiveness improvement achieved by each design alone can be summed.

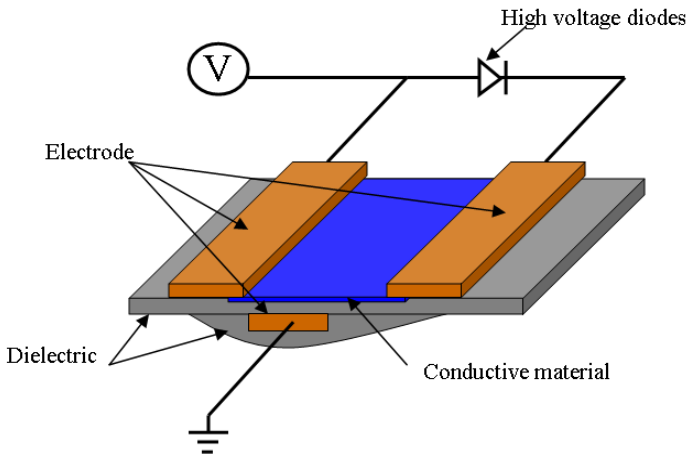

Figure 5.8: Plasma actuator design with an a-silicon film and diodes [29]

Preliminary results for this combined design are shown in Figure 5.9. The dielectric used in this set of experiments was a 0.635 mm (0.025 inch) thick ceramic. These experiments were run at 1.0 kHz with the applied voltage varying from 10 kV to 20 kV peak-to-peak.

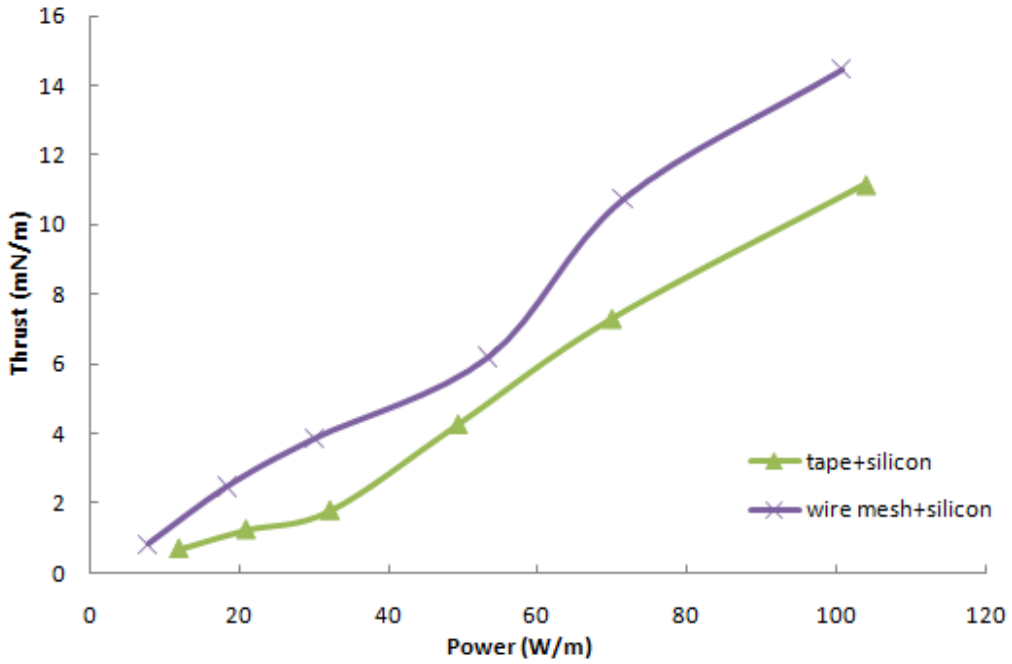

Figure 5.9: Effectiveness for actuator with an a-silicon film and diodes and with different exposed electrodes designs

As shown in Figure 5.9, the mesh wire exposed electrode does improve the thrust from 11.2 mN/m to 14.5 mN/m at an input power of 100 W/m, an improvement of 29% for this alternative combined actuator design. This compares well with the effectiveness improvement achieved when using a mesh exposed electrode on a traditional two-electrode actuator design, suggesting that micro-scale electrodes can be successfully combined with various other design modifications to enhance actuator effectiveness through a cumulative effect.

5.4 Summary

In this section several methods were discussed for manipulating the uniformity of the plasma discharge by modifying the exposed electrode, including using dielectric shielding to cover the exposed electrode, using a deposited exposed electrodes, and using a micro-scale exposed electrode. Preliminary results from testing some of these alternative exposed electrode designs suggest that they can lead to enhanced actuator performance. This is particularly true for micro-scale exposed electrode designs which, in combination with additional actuator design improvements, have the potential to significantly increase plasma actuator effectiveness.

Bibliography

[1] Wisler, DC., “The technical and economic relevance of understanding Blade Row interactions effects in turbomachinery,” von Karman Institute for Fluid Dynamics Lecture series 1998-02, February 9-12 (1998)

[2] Aerospaceweb.org “Golf Ball Dimples & Drag” (2010) http://www.aerospaceweb.org/question/aerodynamics/q0215.shtml

[3] Hourmouziadis J., “Aerodynamic Design of Low Pressure Turbines,” AGARD Lecture Series 167 (1989)

[4] Donovan J.F., Kral L.D., and Cary A.W., "Active Flow Control Applied to an Airfoil," 36th AIAA Aerospace Sciences Meeting and Exhibit, Reno, NV, Jan. 12-15, (1998)

[5] Siemens W., *Poggendorff’s Ann. Phys. Chem*. 102 (1857) 66

[6] Fridman A., Chirokov A. and Gutsol A. “Non-Thermal Atmospheric Pressure Discharges,” *J. Phys. D*. 38(2) (2005) R1- R24.

[7] Kogelschatz U., Eliasson B., and Egli W., "Dielectric-barrier discharges: Principle and applications", *J. Phys. IV* 7 C4 (1997) 47–66.

[8] Kuraica M. M., “Application of Coaxial Dilectric Barrier Discharge for Potable and Waste Water Treatment,” Center for Science and Tech. Development, Serbia and Montenegro (2004)

[9] Kogelschatz U., “Fundamentals and applications of dielectric barrier discharges,” (2000) 1–7

[10] Moreau E., “Airflow control by non-thermal plasma actuators,” *J. Phys. D*. 40 (2007) 605–636.

[11] Gibalov V. and Pietsch G., “The development of dielectric barrier discharges in gas gaps and surfaces,” *J. Phys. D.* 33 (2000) 2618-2636

[12] Golubovskii YuB, Maiorov VA, Behnke J, Behnke JF. “Influence of interaction between charged particles and dielectric surface over a homogeneous barrier discharge in nitrogen,” *J. Phys. D.* 35 (2002) 751–761

[13] Kozlov KV, Wagner H-E, Brandenburg R, Michel P. "Spatio-temporally resolved spectroscopic diagnostics of the barrier discharge in air at atmosperic pressure," *J. Phys. D* 34 (2001) 3164–3176

[14] Madani M., Bogaerts A., Gijbels R., Vangeneugden D. Modelling of a dielectric barrier glow discharge at atmospheric pressure in nitrogen. In *Int. Conf. Phenom. Ionized Gases*, ed. J Meichsner, D Loffhagen, HE (2003)

[15] Pai S.T., Guo X.M., Zhou T.D., “Closed form analytic solution describing glow discharge plasma,” *Phys.Plasmas* 3 (1996) 3842–3852

[16] Corke T., Enloe C., and Wilkinson P., “Dielectric Barrier Discharge Plasma Actuators for Flow Control,” *Annu. Rev. Fluid Mech* 442 (2010) 505–529

[17] Thomas F., Corke T., Iqbal M, Kozlov A, Shatzman D. “Optimization of SDBD plasma actuators for active aerodynamic flow control,” *AIAA J.* (2009) In press.

[18] Forte M., Jolibois J., Pons J., Moreau E., Touchard G. and Cazalens M., “Optimization of a dielectric barrier discharge actuator by stationary and non-stationary measurements of the induced flow velocity: application to airflow control” *Experiments in Fluids* 43 6 (2007) 917-928

[19] Enloe C., McLaughlin E., VanDyken D., and Kachner K., "Mechanisms and Responses of a Single Dielectric Barrier Plasma Actuator: Geometric Effects," *AIAA J.* 42 3 (2004)

[20] Pons J., Moreau E. and Touchard G., "Asymmetric surface dielectric barrier discharge in air at atmospheric pressure: electrical properties and induced airflow characteristics," *J. Phys. D.* 38 (2005) 3635–3642

[21] Hoskinson A., Hershkowitz N. and Ashpis D. "Force measurements of single and double barrier DBD plasma actuators in quiescent air,” *J. Phys. D.* 41 (2008) 245209

[22] Mangolini L.“Experimental and numerical study of dielectric barrier discharges in Helium,” Doctoral dissertation, University of Minnesota, (2002)

[23] Garamoon A. A. and El-zeer D. M.“Atmospheric pressure glow discharge plasma in air at frequency 50 Hz,” *Plasma Sources Sci. Technol.* 18 (2009) 045006

[24] Hoskinson A. and NHershkowitz N., “Flow measurements and plasma simulations of double and single barrier DBD plasma actuators in quiescent air,” 46th AIAA Aerospace Sciences Meeting and Exhibit
AIAA 2008-1370 7 - 10 January, Reno, Nevada (2008)

[25] Enloe C, Font G, McLaughlin T, Orlov D. “Surface potential and longitudinal electric field measurements in the aerodynamic plasma actuator,” *AIAA J.*46 (2008) 2730–2740

[26] Koskinen H., “Plasma collisions and conductivity lecture note,” University of Helsinki, Dept. Of Physics, Finland (2010) theory.physics.helsinki.fi/~xfiles/plasma/07/lect07/Collisions_conductivity.pdf

[27] ITW Paktron, “Type CS4/CS6 Capstic Capacitor Metallized PET Dielectric data sheet,” (2010) http://www.paktron.com/pdf/Capstick_CS4_CS6.pdf

[28] Thomas F.; Corke T., Iqbal M., Kozlov A., Schatzman D., “Optimization of Dielectric Barrier Discharge Plasma Actuators for Active Aerodynamic Flow Control” *AIAA J.* 47 9 (2009) 2169-2178

[29] Guo S., Simon T., Ernie D., and Kortshagen U.,“Separation Control Using DBD Plasma Actuators: Thrust Enhancement Studies,” 48th AIAA Aerospace Sciences Meeting, Orlando, Florida, Jan, (2010)

Appendix A. List of Nomenclature

L – Plasma length
W – Plasma width
T – Dielectric thickness
R_d - Dielectric resistance
C – Dielectric capacitance
R_p - Plasma resistance
σ - Classical conductivity
n_e - Electron density
e - Elementary charge
m_e - Electron mass
σ_n - Impact cross section
$\langle V \rangle$ - Mean velocity
υ_p - Most probable speed
T_e - Electron temperature
A – Plasma area
d – Electrode thickness
ε_r - Relative permittivity
ε_0 - Vacuum permittivity
X – Reactance
ω - Angular frequency
f = Frequency
S – Complex power
P – Real power
Q – Reactive power
Z – Impedance
Z_d- Dielectric Impedance
V_m - Applied voltage magnitude
Z^* - Conjugate of the Impedance
V- Applied voltage peak-to-peak magnitude
$V_{in(p\text{-}p)}$ – Applied voltage peak-to-peak
I – Current
V_pulse - Pulse

Appendix B. MATLAB Code

This code was used in section 4.2 Data Analysis

```
k = 1.381*10^-23; %Boltzmann's constant (J/k)
T_e = 11000; %electron temp (K)
T_i = 300; %ion temp (K)
n_i = 10^15; %ion density (1/cm^3)
n_e = 10^15; % electron density for microdischarge (1/cm^3)
sigma_n=10^-20; % cross section (m^2)
e = 1.6*10^-19; % elementary charge (C)
m_e = 9.11*10^-31; % electron mass (kg)
epsilon_0 = 8.854*10^-12; % vacuum permittivity (F/m)
f = 1*10^3; %frequency (Hz)
omega = 2*pi*f; %Angular frequency
T_0 = 273; %0C = 273K
T_r = 300; %Room temp = 300K
n_0 = 2.69*10^19; % standard number density (1/cm^3)
%=========================
L = 10*10^-3; %Plasma length (m)
W = 9*10^-2; %Plasma width (m)
A = L*W; % Plasma Area
T = 0.3*10^-3; %Dielectric thickness (m)
d = T;
t = 7.62*10^-5 %Electrode tape thickness (m)
A_c = W*t;
%=========================
%netural density (1/cm^3)
n_n = n_0*T_0/T_r

%degree of ionization
alpha = n_i/(n_i+n_n)

%mean velocity
v = 2/(pi)^0.5*(2*k*T_e/m_e)^0.5

%collusion frequency
nu_n = n_n*10^6*sigma_n*v

% classical conductivity = sigma (S/m)
sigma = n_e*10^6*e^2/(m_e*nu_n)

%plasma resistance (ohm)
R_p = L*0.5/(sigma*A_c)
% R_test = L/(sigma*

%Dielectric capacitance
C = epsilon_r*epsilon_0*A/d
```

```
%Dielectric impedence (ohm)
Z = 1/(omega*C)

%PET resistivity (ohm.m)
% rho_d = 10^20
rho_d = 10^10
%resistant of dielectric
% R_d = d*rho_d/A
R_d = 1*10^9
%=================================
x = R_d/(1+(R_d*omega*C)^2)
R_de = x
X_de = -x*R_d*omega*C
R_e = (R_p+x)/((R_p+x)^2+(x*R_d*omega*C)^2)
X_e = (-x*R_d*omega*C)/((R_p+x)^2+(x*R_d*omega*C)^2)

P = 10000^2/2*R_e
Q = 10000^2/2*X_e
```